Ovarian development is driven by early spatiotemporal priming of the coelomic epithelium

Authors: Cyril Djari[1,2,†], Chloé Mayère[1,2,†], Maëva Guy[1,2], Aitana Perea-Gomez[3], Paul Barreau[1,2], Agathe Rozier[3], Anthony S. Martinez[4], Tyler J. Gibson[4], Cassandre Guérin[3], Herta Ademi[1,2], Dagmar Wilhelm[5], Jennifer McKey[4], Marie-Christine Chaboissier[3], Serge Nef[1,2,*].

Affiliations:

[1]Department of Genetic Medicine and Development, University of Geneva, 1211 Geneva, Switzerland.

[2]iGE3, Institute of Genetics and Genomics of Geneva, University of Geneva, Switzerland.

[3]Université Côte d'Azur, Inserm, CNRS, Institut de Biologie Valrose (iBV), 06108 Nice, France.

[4]Section of Developmental Biology, Department of Pediatrics, University of Colorado Anschutz Medical Campus, Aurora, CO, 80045, USA.

[5]Department of Anatomy & Physiology, University of Melbourne, VIC 3010, Australia.

[†]These authors share first authorship

[*]Corresponding Author: Email: Serge.Nef@unige.ch

Abstract

Ovarian organogenesis requires the coordinated specification of supporting and steroidogenic cell lineages from multipotent coelomic epithelium (CE) progenitors. A longstanding question is whether the CE contains transcriptionally distinct, spatially organized progenitor subpopulations with predetermined lineage biases, or whether specification into supporting and steroidogenic lineages occurs only after delamination and integration into the bipotential gonad. The developmental origins of granulosa cells and the emergence of ovarian steroidogenic/stromal progenitors (SPs) also remain poorly defined. Here, we show that CE cells covering the fetal mouse ovary are transcriptionally heterogeneous and spatially organized into subdomains already primed toward supporting or steroidogenic fates. CE priming is dynamic, with transient coexistence of supporting- and steroidogenic-biased CE progenitors before resolving into a predominantly supporting-biased CE. Local delamination of these primed cells seeds intragonadal niches where pre-granulosa cells and SPs mirror the spatio-temporal arrangements of CE-primed progenitors. We further demonstrate a dual origin for the supporting lineage, with granulosa cells deriving from both the CE and supporting-like cells (SLCs). In parallel, we show that SPs arise from steroidogenic-primed CE cells, expand to represent 52% of ovarian somatic cells at birth, persist into adulthood and contribute to both theca and steroidogenic stromal cells. Together, these findings reveal transcriptionally and spatially distinct CE subpopulations that shape somatic lineage emergence with important implications for ovarian pathophysiology.

Keywords: Ovarian development; coelomic epithelium; ovarian surface epithelium; granulosa cells; steroidogenic/stromal progenitors; theca cells; single-cell RNA-sequencing (scRNA-seq); spatial transcriptomics; lineage tracing; fate restriction.

Introduction

In mice, the gonadal primordium arises from the lateral plate mesoderm (Neirijnck et al., 2023; Qiu et al., 2024). By embryonic day (E) 9.5, proliferating CE progenitors overlying the mesonephros expand rapidly, contributing to gonad formation in both XX and XY embryos. This expansion is driven by asymmetric divisions, whereby some daughter cells remain in the CE, while others undergo epithelial-to-mesenchymal transition (EMT) and ingress into the gonad (Karl and Capel, 1998; Kusaka et al., 2010; Lin et al., 2017; Schmahl et al., 2000). NUMB, a NOTCH antagonist, is asymmetrically localized in CE cells and is required for polarity and asymmetric divisions that direct CE progenitors toward gonadal somatic fates (Lin et al., 2017). CE-derived cells give rise to the three major gonadal somatic cell lineages: supporting, steroidogenic/stromal, and supporting-like cells (SLCs) (Ademi et al., 2022; Capel, 2000; DeFalco et al., 2011; Garcia-Alonso et al., 2022; Karl and Capel, 1998; Liu et al., 2016; Mayere et al., 2022; Mork et al., 2012; Schmahl and Capel, 2003; Stevant et al., 2019; Stevant and Nef, 2018). The supporting lineage gives rise to pre-granulosa cells in XX gonads and Sertoli cells in XY gonads, while the steroidogenic lineage forms theca/stromal steroidogenic and Leydig cells, respectively. SLCs are specified as early as E10.5, before gonadal sex determination, and contribute to the rete ovarii and rete testis, and a subset of supporting cells (Mayere *et al.*, 2022; McKey et al., 2022). A central unresolved question is whether the CE contains transcriptionally distinct and spatially organized progenitor subpopulations that are already biased toward supporting or steroidogenic fates, or whether lineage specification occurs only after progenitor ingression into the bipotential gonad.

Other fundamental unresolved questions in ovarian development concern the potential dual origins of pre-granulosa cells and the specification of SPs. Pre-granulosa cells arise in two successive waves: a first wave of intragonadal FOXL2^{+} supporting cells around the time of gonadal sex determination that gives rise to granulosa cells of medullary follicles (Mork *et al.*, 2012; Niu and Spradling, 2020; Zheng et al., 2014), and a second wave derived from *Lgr5*$^{+}$ progenitors in the surface epithelium from E14.5 onward that contributes to cortical follicles (Cai et al., 2020; Feng et al., 2016; Niu and Spradling, 2020; Rastetter et al., 2014; Stevant *et al.*, 2019). Despite these insights, the dynamics of these successive waves of pre-granulosa cell differentiation in the developing ovary remain poorly understood, as does the contribution of other cell types. In particular, XX SLCs were shown to give rise to both the rete ovarii and a subset of pre-granulosa cells (Mayere *et al.*, 2022; McKey *et al.*, 2022), but the magnitude, regional distribution between medulla and cortical compartments, and persistence of this contribution remain unresolved. For the steroidogenic lineage, theca cells first appear around one week after birth in secondary follicles, coinciding with LH responsiveness and activation of steroidogenic enzymes expression (Magoffin

86 and Weitsman, 1994). Lineage tracing studies identified two sources of SPs: migratory mesonephric
87 cells and WT1^{+} intraovarian stromal cells (Liu et al., 2015), which remain undifferentiated during
88 fetal life and differentiate as theca cells postnatally in response to granulosa-derived DHH/IHH
89 signals (Cowan and Quirk, 2021; Liu *et al.*, 2015; Richards et al., 2017). Although ovarian
90 steroidogenic cells likely share common progenitor features with their testicular counterparts, how
91 ovarian SPs are specified, maintained until perinatal follicle activation, and subsequently
92 differentiate into theca cells remain poorly understood.
93 To address these fundamental questions, we employed single-cell RNA sequencing, spatial
94 transcriptomics, immunofluorescence, and inducible lineage tracing to investigate early
95 specification of CE progenitors, trace the origins of pre-granulosa cells, and characterize the
96 emergence and fate of SPs in the developing ovary. We show that CE progenitors are
97 transcriptionally heterogeneous as early as E11.5, with subpopulation already biased toward
98 supporting or steroidogenic/stromal fates. These primed populations are spatially organized along
99 the ovarian surface and mirror the intragonadal distribution of their corresponding lineages. We
100 further demonstrate that fetal intraovarian SPs give rise to adult steroidogenic theca and stromal
101 cells, and that granulosa cells originate from both CE and SLCs with region-specific contribution.
102 Together, these findings reveal that spatially organized CE subpopulations directly seed ovarian
103 lineages through local delamination, establishing distinct intragonadal niches with important
104 implications for ovarian pathophysiology.
105

106 **Results**

107 **A comprehensive single-cell transcriptomic atlas of mouse ovarian development**

108 We combined available datasets to generate a comprehensive single-cell RNA-sequencing (scRNA-
109 seq) atlas spanning mouse ovarian development from embryonic day (E)10.5 to adulthood (P56)
110 (**Fig. 1A**). This atlas covers ten developmental stages (E10.5, E11.5, E12.5, E13.5, E14.5, E16.5,
111 E18.5, P1, P5, and P56), thereby capturing the major transitions underlying gonadal sex
112 determination and early ovarian development. The atlas integrates data from three published
113 studies, including two generated in our laboratory (Mayere et al., 2022; Niu and Spradling, 2020;
114 Rossitto et al., 2022). After applying uniform quality control procedures across all datasets (see
115 Materials and Methods), we retained 68,366 high-quality cells for downstream analyses (**Fig. 1B**).
116 To resolve cellular identities with high accuracy, we first analyzed each developmental stage
117 independently. UMAP embedding and Leiden clustering revealed consistent and reproducible
118 structure across biological replicates (**Fig. S1A–B**). Marker gene expression enabled the
119 identification of all major gonadal and mesonephric cell types, including coelomic/surface

epithelium (abbreviated CE/SE; *Gata4*$^{+}$/*Upk3b*$^{+}$; CE up to E16.5, SE after E16.5), supporting-like cells (SLCs; *Pax2*$^{-}$/*Pax8*$^{+}$), pre-supporting cells (pre-Sup; E11.5; *Wnt6*$^{+}$), pre-granulosa cells (pre-Gran; E12.5-P1; *Foxl2*$^{+}$), granulosa cells (Gran; P5-P56; *Foxl2*$^{+}$), gonadal mesenchyme (GM; *Gata4*$^{+}$/*Tcf21*$^{+}$/*Wnt6*$^{-}$), stromal progenitors (SPs; *Gata4*$^{+}$/*Tcf21*$^{+}$), steroidogenic cells (Stero; P5-P56; *Cyp11a1*$^{+}$), smooth muscle cells (SM; *Myh11*$^{+}$), luteal cells (Luteal; *Mrap*$^{+}$), perivascular cells (PV; *Rgs5*$^{+}$), germ cells (Germ; *Dazl*$^{+}$), mesonephric mesenchyme (MM; *Gata4*$^{-}$/*Gata2*$^{+}$), mesonephric tubules (MT; *Pax2*$^{+}$/*Pax8*$^{+}$), adrenosympathetic cells (AS; *Phox2b*$^{+}$), endothelial cells (End; *Cdh5*$^{+}$), erythrocytes (Eryt; *Rhd*$^{+}$), and immune cells (Immune; *Cd52*$^{+}$) (**Fig. S1C and S1D**). The stage-specific datasets/annotations were then integrated into a unified atlas capturing the dynamic transcriptional landscape of ovarian development (**Fig. 1C-F**). This atlas provides a comprehensive framework for reconstructing ovarian somatic lineage trajectories across embryonic and postnatal stages and for exploring the mechanisms that govern ovarian cell fate decisions. An interactive viewer is available for further exploration [https://www.unige.ch/medecine/nef/datasets].

Dual origins of pre-granulosa cells revealed by somatic lineage trajectories

To investigate the specification and differentiation dynamics of the two major somatic lineages of the ovary, the supporting and steroidogenic lineages, we generated a sub-atlas restricted to relevant ovarian somatic cell populations. This included early gonadal progenitors (CE and GM), supporting lineages cells (pre-Sup, pre-Gran, and Gran), supporting-like cells (SLCs) and steroidogenic lineage cells (SP, Stero, SM, and PV). To reduce cellular complexity and improve interpretability, we excluded systemic cell types (immune, erythrocytes, endothelial), luteal cells, germ cells, and early mesonephric populations. Partition-based Graph Abstraction with conductance scoring (cPAGA) confirmed that CE/SE progenitors constitute a central developmental node, strongly connected to both granulosa and steroidogenic lineages, while also highlighting a robust transcriptional link between SLCs and pre-granulosa cells (**Fig. 1G**). Stage-specific analyses from E11.5 to P5 confirmed that pre-granulosa cells maintained strong connections with CE/SE and SLCs throughout development, whereas stromal progenitors disconnected from CE at E16.5 (**Fig. 1H**). UMAP embedding of the somatic sub-atlas confirmed these links between cell populations, with temporally ordered, continuous trajectories consistent with lineage progression (**Fig. 1I** and **J**). Thus, CE/SE progenitor cells followed two principal developmental trajectories: one toward the supporting lineage and another toward the steroidogenic lineage. In addition, a distinct trajectory originating from SLCs also contributed to the supporting lineage. As expected, cell type proportions shifted across development: CE/SE and SLC cells made up a high proportion of cells at E11.5 but this

154 percentage declined thereafter (42.4% and 8.8% at E11.5 vs 4.4% and 0.5% at P5), while the
155 proportion of supporting and SP cells progressively expanded (35.7% and 13.1% at E11.5 vs 42.5%
156 and 45.9% at P5) (**Fig. 1K**). Cell cycle analysis revealed that CE/SE cells were highly proliferative
157 during early stages, with proliferation declining over time (**Fig. 1L**). By contrast SPs were highly
158 proliferative at early stages, aligning with their expansion in the gonad, whereas pre-granulosa cells
159 remained largely quiescent throughout fetal development as described before (Gustin et al., 2016;
160 Mork *et al.*, 2012). Together, these findings indicate that pre-granulosa cells arise from two
161 transcriptionally distinct progenitor sources, CE and SLCs. This dual origin challenges the classical
162 model of an exclusively CE-derived lineage and introduces the concept of convergent granulosa
163 cell differentiation.
164

165 **Coelomic epithelial cells and supporting-like cells give rise to pre-granulosa cells**

166 To confirm the dual origin of pre-granulosa cells, we performed *in vivo* lineage tracing using
167 complementary strategies targeting either CE or SLCs and tracked their contribution to the FOXL2$^+$
168 granulosa cell population from fetal (E12.5) to adult stages (8 weeks).
169 We first identified *Wnt5a* as a CE marker between E11.5 and E12.5 (**Fig. 2A-D**). Although *Wnt5a*
170 is expressed in SPs, during this developmental window its expression within the supporting lineage
171 was confined to CE and absent from pre-granulosa cells. To trace CE-derived cells, we used *Wnt5a-*
172 *rtTA;TetO-Cre;Rosa-tdTomato* mice (hereafter *Wnt5a^{lin}*) (Ademi *et al.*, 2022), and induced Cre
173 expression with doxycycline between E11.5-E12.5 (**Fig. 2E** and **F**). At E12.5, tdTomato labelled
174 efficiently most of the CE cells (**Fig. 2G**). At this stage, 25.3% of FOXL2$^+$ cells co-expressed
175 tdTomato (**Fig. 2H**). This proportion increased substantially by E16.5, comprising 52.6% of the
176 pre-granulosa cells, and further expanded to 65.7% by adulthood (**Fig. 2I** and **J**).
177 tdTomato$^+$/FOXL2$^+$ granulosa cells were primarily localized in the cortical region at both E16.5
178 and P5, consistent with a CE-derived origin of cortical granulosa cells.
179 To trace the SLC lineage, we used the *Pax8-Cre;Rosa-tdTomato* mice (hereafter *Pax8^{lin}*) (Mayere
180 *et al.*, 2022), as *Pax8* is a specific marker of SLCs and rete ovarii (**Fig. 2K-N**). The *Pax8^{lin}* system
181 is constitutive, therefore, we first confirmed that *Pax8* expression remains restricted to the SLC/rete
182 ovarii throughout fetal and postnatal development, validating lineage specificity (**Fig. 2O-P, Fig.**
183 **S2A and S2B**). We previously showed that SLC give rise to a small proportion of supporting cells
184 in newborn mice (Mayere *et al.*, 2022). Here, we show that at E12.5, tdTomato$^+$ cells were confined
185 to the SLCs, and absent from both CE and FOXL2$^+$ granulosa cells (**Fig. 2Q** and **R**). By E16.5,
186 however, 22.4% of FOXL2$^+$ pre-granulosa cells were tdTomato$^+$, and these were located
187 predominantly in the medulla . At P5, region-specific quantification showed SLC-derived granulosa

188 cells were present in comparable proportions in the cortical and medullary compartments (**Fig. 2S,**
189 **Fig. S2C** and **S2D**). Immunofluorescence revealed a tdTomato^{+}/FOXL2^{+} gradient across the ovary
190 with the highest number of positive cells near the ovarian hilum, consistent with a contribution from
191 SLC/rete ovarii cells. By adulthood, this contribution declined to 10.3%, indicating that SLC-
192 derived granulosa cells represent a transient population active mainly during fetal development and
193 early folliculogenesis (**Fig. 2S** and **2T**).
194 Together, these lineage tracing experiments provide *in vivo* evidence that granulosa cells originate
195 from two spatially distinct progenitor pools. CE-derived cells represent the major source, giving
196 rise primarily to cortical granulosa cells, while SLC-derived cells contribute to a transient medullary
197 subset and a minor cortical subpopulation. These findings confirm the dual trajectories identified
198 by scRNA-seq from CE and SLCs, and refine the classical model of a single CE-derived granulosa
199 lineage.
200

201 **Transcriptional heterogeneity reveals early fate priming in the coelomic epithelium**

202 Consistent with previous studies showing that CE progenitors contribute to both supporting and
203 steroidogenic and lineages (see Introduction), our atlas revealed strong transcriptional continuity
204 between CE/SE and both somatic cell fates (**Fig. 3A**). However, it remains unclear whether the CE
205 overlying the developing gonad is already heterogenous, containing transcriptionally distinct fate-
206 biased subpopulations, or whether it is initially homogeneous and multipotent until lineage
207 restriction occurs after ingression into the gonadal mesenchyme. To address this question, we re-
208 analyzed ovarian somatic cells from E10.5 to P56, focusing on CE/SE and their derived cells.
209 CE/SE identity was confirmed by *Upk3b* expression; supporting cells by *Bmp2, Irx3, Lgr5, Runx1*
210 and *Wnt6;* and SPs by *Arx, Nr2f2, Pdgfra* and *Tcf21* (**Fig. 3B** and **Fig. S3**). Strikingly, these markers
211 were also expressed in CE/SE cells, either in mutually exclusive or overlapping patterns, indicating
212 transcriptional heterogeneity and suggesting early fate priming. To assess CE/SE fate biases
213 without relying on individual markers, we computed supporting- and stromal-identity scores for
214 each CE/SE cell using lineage-specific transcriptomic signatures. UMAP color-coded by scores
215 revealed CE/SE subpopulations with distinct fate biases: supporting-biased CE/SE cells with high
216 supporting scores clustered near the supporting cells, whereas stromal-biased CE/SE cells with high
217 stromal scores clustered near the SP population (**Fig. 3C**). CE/SE cells with low scores for both
218 occupied a transitional zone within the CE/SE cluster. As expected, stromal-biased CE/SE cells
219 expressed SP markers (*Arx*, *Pdgfra*, *Nr2f2*, and *Tcf21*), whereas supporting-biased CE/SE cells
220 expressed supporting markers (*Bmp2, Irx3, Lgr5, Runx1* and *Wnt6*) (**Fig. 3B** and **Fig. S3**). Based
221 on scores, we classified CE/SE cells into two categories: supporting-biased cells (supporting >

222 stromal) and stromal-biased cells (stromal > supporting) (**Fig. 3D**). Differential gene expression
223 between supporting- and stromal-biased CE/SE cells identified 4,761 differentially expressed genes
224 (DEGs), 94% of which overlapped with the 9,976 genes differentially expressed between
225 supporting and stromal cell populations (**Fig. 3E** and **Data S1**). Thus, the CE is not a uniform
226 progenitor pool, it comprises transcriptionally distinct subpopulations already biased toward
227 steroidogenic or supporting fates. These primed CE subpopulations display transcriptomic profiles
228 closely resembling their respective target lineages.
229
230 **Temporal dynamics of coelomic epithelium priming**
231 To track the dynamics of CE priming, we analyzed CE/SE cells across eight development stages,
232 from the onset of somatic lineages specification (E11.5) through differentiation into pre-granulosa
233 cells and SPs (P5). At each stage, stromal and supporting identity scores were computed for
234 individual CE/SE cells, revealing three phases of CE/SE fate bias (**Fig. 3F**). At E11.5, CE cells
235 exhibited low stromal and supporting-identity scores, consistent with a largely unbiased state.
236 Between E12.5 and E14.5, supporting- and stromal-biased CE subpopulations coexisted. By E16.5,
237 CE cells were predominantly biased toward the supporting fate, with the stromal-biased CE subset
238 lost. These transitions were accompanied by a progressive decline in stromal-identity score and a
239 sustained increase in supporting-identity score (**Fig. 3G**). Marker expression confirmed these
240 dynamics (**Fig. 3H**). At E11.5, a high proportion of CE cells expressed SP markers (*Arx, Pdgfra,*
241 *Nr2f2, Tcf21*). Between E12.5 and E14.5, expression became more balanced, with supporting
242 marker expression (*Bmp2, Irx3, Lgr5, Runx1, Wnt6*) increasing as SP marker expression declined.
243 From E16.5 to P5, most CE/SE cells expressed supporting lineage markers. Stage-wise cPAGA
244 further indicated that CE cells remained transcriptionally connected to both supporting and
245 steroidogenic lineages during the bipotential window (E12.5 and E14.5) but became exclusively
246 linked to the supporting lineage from E16.5 onward (**Fig. 1H**). Consistently, conductance scores
247 reflecting CE connectivity to the steroidogenic lineage dropped sharply after E14.5, while CE/SE-
248 supporting connectivity persisted until P5 (**Fig. 3I**).
249 Together, these findings revealed transcriptionally distinct subpopulations already biased toward
250 supporting or stromal fates. Early priming within the CE likely shapes downstream differentiation
251 and the spatial organization of ovarian somatic lineages, suggesting that lineage potential is pre-
252 patterned before integration into the gonadal mesenchyme.
253
254 **Dynamic spatial patterning of primed-coelomic epithelial cells**

255 Having identified supporting- and steroidogenic-primed CE subpopulations, we next analyzed their
256 dynamic spatial organization during development. For this, we used spatial transcriptomics data
257 generated with 10x Genomics Visium HD technology on parasagittal sections of XX gonads at
258 E12.5, E14.5, and E16.5 (**Fig. 4A**;(Martinez et al., 2025)). Data were binned at 4µm and annotated
259 using a logistic-regression model trained on our single-cell transcriptomic atlas. Gonadal and CE
260 regions were annotated by *Gata4* and *Upk3b* expression, respectively. To assess spatial
261 organization within the CE, we constructed an anteroposterior pseudo-spatial axis. Supporting- and
262 stromal-identity scores were then calculated along the pseudo-spatial axis to localize fate-biased
263 CE subpopulations (**Fig. 4B**). At E12.5, steroidogenic bias was enriched at the extremities of the
264 pseudo-spatial axis near the gonad-mesonephros junction, whereas supporting bias concentrated
265 centrally. This regionalization persisted at E14.5 but became less distinct by E16.5 as the stromal
266 signature declined. Heatmap analysis of genes enriched in supporting-biased (n = 340) and stromal-
267 biased (n = 273) CE cells further confirmed this spatial segregation (**Fig. 4C, Fig. S4A** and **Data**
268 **S1**). In particular, steroidogenic-biased CE cells at the extremities of the pseudo-spatial axis
269 expressed *Nr2f2*, *Tcf21*, *Pdgfra* and *Pdgfrb*, whereas supporting-biased CE cells in the central
270 region expressed *Runx1*, *Wnt6*, *Bmp2*, *Irx3*, *Irx5*, *Lgr5*, and *Fst* (**Fig. 4D** and **Fig. S4B**).
271 To further refine the spatial dynamics of CE subpopulations, we performed combined *in situ*
272 hybridization (ISH) and immunofluorescence (IF) on XX gonads from E12.5 to E16.5. Alongside
273 the CE/SE marker *Upk3b*, we detected supporting lineage markers *Bmp2* and RUNX1, and the SP
274 marker NR2F2, all previously identified in CE subpopulations by our transcriptomic analyses (**Fig.**
275 **3H** and **Fig. S3**). At E12.5 and E13.5, ISH/IF confirmed distinct spatial domains of supporting- and
276 steroidogenic-primed CE cells along the ovarian surface (**Fig. 4E** and **S4C**). On transverse sections,
277 NR2F2$^+$ cells localized within the CE at the gonad-mesonephros junction, whereas RUNX1$^+$ and
278 *Bmp2*$^+$ cells were restricted to the central CE. These regions also exhibited distinct epithelial
279 morphologies: the NR2F2$^+$ domain appeared pseudostratified and columnar, while
280 RUNX1$^+$/*Bmp2*$^+$ domain was cuboidal or squamous, as confirmed by β-Catenin and Laminin A1
281 staining (**Fig. 4F**). By E16.5, NR2F2 was no longer detectable in the CE, while RUNX1$^+$ was
282 uniformly expressed, consistent with an exclusive supporting-bias beyond this stage (**Fig. S4C**).
283 Notably, *Bmp2* expression declined in both CE and supporting-lineage cells between E13.5 and
284 E16.5, whereas other supporting markers (*Irx3*, *Lgr5*, *Runx1* and *Wnt6*) remained highly expressed,
285 indicating that *Bmp2* expression is transient (**Fig. 3H, Fig. S3** and **Fig. 4E**). To determine the onset
286 of spatial patterning, we analyzed E11.5 gonads and observed widespread NR2F2 in the CE, no
287 detectable RUNX1, and *Bmp2* restricted to the central CE, suggesting that positional bias emerges
288 within the CE before the onset of granulosa cell differentiation (**Fig. S4D and S4E**). Together, these

289 findings demonstrate that CE fate bias is encoded both transcriptionally and spatially, providing a
290 framework for understanding how progenitor positioning influences the emergence of distinct
291 somatic lineages in the fetal ovary.
292

293 **Spatial priming of the coelomic epithelium predicts supporting and steroidogenic lineage**
294 **commitment**

295 Having established spatially distinct primed CE domains, we next asked whether these regions seed
296 the corresponding intragonadal lineages. We observed intra-ovarian NR2F2^{+} and *Bmp2*$^{+}$ cells
297 directly beneath their respective CE regions, suggesting that primed CE subpopulations delaminate
298 locally to contribute to pre-granulosa and SPs (**Fig. 4E**, at E13.5). Spatial transcriptomics further
299 revealed that intragonadal distributions of pre-granulosa cells/SLCs and SPs mirror the spatio-
300 temporal arrangements of CE-primed progenitors: regions beneath stromal-primed CE at the
301 extremities of the pseudo-spatial axis contained higher proportions of SPs, whereas areas beneath
302 supporting-biased CE in the central region were enriched for supporting cells (**Fig. 4G**). LAMA1
303 staining revealed focal discontinuities in the basal lamina beneath both stromal- and supporting-
304 biased CE, consistent with EMT-mediated entry into the gonad (**Fig. 4F**). These findings support a
305 direct, spatially organized contribution of CE subpopulations to their corresponding supporting and
306 stromal/steroidogenic lineages.

307 Finally, we leveraged the restriction of CE fate toward the supporting lineage between E14.5 and
308 E16.5 to identify markers of late-gestation SPs. By E16.5, *Wnt5a* expression is confined to SPs,
309 enabling specific labeling in *Wnt5a*^{lin} mice. Doxycycline induction in *Wnt5a*^{lin} mice at E15.5-E16.5
310 confirmed restricted labeling of SPs at E16.5 (**Fig. 2B, 2D, 4H** and **4I**). To trace their fate, we
311 performed *in vivo* lineage tracing and induced *Wnt5a*^{lin} mice at E15.5-E16.5 and analyzed adult
312 ovaries (**Fig. 4H** and **J**). Labeled SPs did not contribute to FOXL2^{+} granulosa cells but gave rise to
313 long-lived adult steroidogenic populations, including CYP11A1^{+} steroidogenic theca and stromal
314 cells. Thus, spatially primed-CE cells delaminate locally to seed distinct intragonadal niches,
315 suggesting that supporting-biased CE cells give rise to pre-granulosa cells, whereas steroidogenic-
316 biased CE cells generate fetal SPs that either differentiate into steroidogenic stromal and theca cells
317 or persist as long-lived adult SPs.
318

319 **Discussion**

320 During early gonadogenesis, proliferating CE cells give rise to most somatic cells in both XX and
321 XY gonads. Classical dye-based labeling, genetic lineage tracing, and single-cell transcriptomics
322 have established that CE progenitors are multipotent, contributing to additional CE cells as well as

323 both supporting and steroidogenic lineages (Ademi et al., 2022; DeFalco et al., 2011; Karl and
324 Capel, 1998; Liu et al., 2016; Mayere et al., 2022; Mork et al., 2012; Schmahl et al., 2003; Stevant
325 and Nef, 2018, 2019). Yet, the events directing CE progenitors into these divergent lineages remain
326 poorly defined. Specifically, it has been unclear whether the CE contains transcriptionally distinct,
327 spatially resolved subpopulations with progenitors already primed toward specific lineages, or
328 whether specification occurs only after CE cells delamination and integration into the bipotential
329 gonad. Recent work on adrenogonadal primordium separation revealed that CE cells are specified
330 toward adrenal or gonadal fates earlier than expected, before their ingression into the underlying
331 mesenchyme (Neirijnck *et al.*, 2023). Notably, even prior to the anatomical separation of the
332 adrenogonadal primordium into cranial adrenal and caudal gonadal domains, CE cells already
333 exhibit transcriptional biases toward adrenal versus gonadal lineages. These findings argue that
334 specification within the CE can precede ingression and may involve spatial pre-patterning of
335 progenitor identity.
336 Here, we provide an integrative single-cell and spatial framework of mouse ovarian development
337 from genital ridge formation (E10.5) to adulthood (P56) and present a revised model of somatic
338 lineage specification. By combining a developmental scRNA-seq atlas with *in vivo* lineage tracing
339 and spatial transcriptomics, we show: (1) transcriptional heterogeneity and temporal priming within
340 CE as early as E11.5, (2) spatial organization of these primed states along the CE, (3) local
341 delamination of spatially primed CE cells to seed distinct intragonadal niches, and (4) a dual origin
342 of granulosa cells from CE cells and SLCs. Together, these findings define the spatiotemporal
343 program of ovarian somatic lineages specification and establish a foundation for mechanistic and
344 translational studies.
345

346 **Early heterogeneity and spatiotemporal dynamic of coelomic epithelium priming**

347 CE progenitor cells overlying the developing ovary are heterogeneous, comprising spatially
348 localized subpopulations already primed toward supporting or steroidogenic fates (model in **Fig.**
349 **5**). One subset co-expresses the epithelial marker *Upk3b* with steroidogenic markers *(Arx, Nr2f2*,
350 *Pdgfra*, and *Tcf21*), whereas another co-expresses *Upk3b* with supporting lineage markers (*Bmp2*,
351 *Irx3*, *Lgr5*, *Runx1* and *Wnt6)*. Differential expression analysis further confirmed that supporting-
352 biased and steroidogenic-biased CE cells exhibit transcriptomic profiles closely resembling their
353 respective target lineages, providing evidence of bona fide priming (**Fig. 3E**).
354 CE priming emerges early and displays regional patterning. At E11.5, most epithelial cells are
355 NR2F2^{+}, with a subset already *Bmp2*$^{+}$, marking the onset of a positional bias. Between E12.5 and
356 E13.5, *Upk3b*$^{+}$/*Bmp2*$^{+}$ supporting-primed CE cells expand across the ovarian surface, whereas

357 *Upk3b*$^{+}$/NR2F2^{+} steroidogenic-primed CE cells remain confined near the mesonephros.
358 Transcriptomic and IF/ISH analyses revealed a gradual transition along the CE rather than a sharp
359 boundary. NR2F2 expression decreases with distance from the mesonephros, while supporting
360 marker expression increases, yielding a continuum of CE cells shifting from steroidogenic to
361 supporting bias. By E16.5, CE cells are almost exclusively supporting-primed (*Upk3b*$^{+}$/*Bmp2*$^{+}$),
362 likely contributing to pre-granulosa cells and, postnatally, to the ovarian surface epithelium. Intra-
363 ovarian NR2F2^{+} steroidogenic progenitors and *Bmp2*$^{+}$ pre-granulosa cells are found directly
364 beneath their respective CE-primed progenitors, consistent with local delamination from spatially
365 distinct CE subdomains. Spatial transcriptomic confirmed that intra-ovarian distribution mirrors
366 CE priming: SPs predominate beneath steroidogenic-primed CE at the pseudo-spatial axis
367 extremities, while supporting cells arise from centrally located supporting-primed CE. These
368 findings support a direct, spatially organized contribution of CE subpopulations to ovarian lineages
369 through local delamination of primed CE progenitors seeding distinct intragonadal niches.
370 Consistent with our finding, Bunce et al. reported a center-biased ingression of supporting cell
371 progenitors in both XX and XY gonads, leading to higher supporting cell density in the central
372 domain of the gonad (Bunce et al., 2023). They showed that *Runx1*, a transient marker of pre-
373 supporting cells, is faintly detectable in CE cells and strongly upregulated upon ingression (Bunce
374 et al., 2023). Using a *Runx1-EGFP* reporter (Gong et al., 2003), they observed greater quantity of
375 GFP cells in the center of the gonad compared with the poles, revealing that supporting cell
376 precursor ingression is center biased during establishment of the pre-supporting cell population in
377 both sexes. In line with this, our NR2F2/RUNX1 double IF at E11.5 revealed that while most CE
378 cells are NR2F2^{+}, faint RUNX1^{+}/NR2F2^{-} CE cells are already detectable in the central part of the
379 XX gonad (**Fig**. **S4E**). These observations raise also the question of transcriptomic priming and
380 regional patterning of CE progenitors in XY gonads during the process of sex determination.
381

382 **Mesonephros-gonad crosstalk as a positional regulator of coelomic epithelial fate**

383 From E12.5 onward, supporting-biased CE cells expand across the ovarian surface, while
384 steroidogenic-biased cells remain confined near the mesonephros, suggesting that local cues
385 promote or maintain steroidogenic fate during the temporal window when both subpopulations
386 coexist. As the ovary enlarges and the CE becomes physically separated from the mesonephros, the
387 steroidogenic-biased CE signature declines, and by E16.5 priming is restricted to the supporting
388 fate. These observations support a model in which mesonephric proximity provides positional cue
389 favoring stromal bias and/or preventing supporting specification. This hypothesis is consistent with
390 the broader paradigm that mesonephros influences gonadal development through cell migration and

391 paracrine signaling. In the testis, mesonephric cells contribute to the interstitium and vasculature,
392 and SPs derive from both CE and mesonephric sources (Ademi et al., 2022; DeFalco et al., 2011;
393 Karl and Capel, 1998; Kumar and DeFalco, 2018; Liu et al., 2016; Rotgers et al., 2018). In the
394 ovary, theca cells originate from a combination of migratory *Gli1*$^{+}$ mesonephric cells and
395 intraovarian SPs, with minor mesonephric input (Liu *et al.*, 2015). Regional differences in CE
396 architecture (pseudostratified vs. cuboidal) further suggest that tissue mechanics or polarity may
397 also bias fate decision.
398
399 **Conserved sequence and sex-specific timing of steroidogenic lineage differentiation**
400 In mammals, testicular and ovarian differentiation follow distinct temporal trajectories, with testis
401 differentiating earlier and more rapidly (Nicol et al., 2022; Stevant and Nef, 2019; Wilhelm et al.,
402 2013). This divergence is most evident in androgen-producing cells: fetal Leydig cells (FLCs)
403 secrete androgens from E12.5 onwards, whereas thecal cells appear only postnatally and produce
404 androgens in response to luteinizing hormone (LH) during folliculogenesis (Barsoum and Yao,
405 2010; Fortune and Armstrong, 1977; Magoffin, 2005; Mannan and O'Shaughnessy, 1991). Despite
406 these timing differences, the specification, expansion, and differentiation of steroidogenic lineages
407 are broadly conserved across sexes.
408 Our data reveal a trajectory in which a subset of CE cells acquires a steroidogenic-primed identity
409 during a restricted developmental time window (E11.5–E14.5) and contributes directly to
410 intraovarian SPs. These SPs proliferate actively and express canonical markers (*Arx*, *Pdgfra*, *Nr2f2,*
411 and *Tcf21*), also shared by testicular SPs (Brennan et al., 2003; Cui et al., 2004; Eliveld et al., 2019;
412 Estermann et al., 2025; Ge et al., 2006; Kilcoyne et al., 2014; Miyabayashi et al., 2013; Perea-
413 Gomez et al., 2025; Qin et al., 2008; Shen et al., 2021). In the ovary, their proportion rise from
414 7.6% at E12.5 to 41.9% by P5, with 50.9% persisting into adulthood (**Fig. 1K**), paralleling the
415 dynamics in the developing testis where SPs are also predominant at birth (Ademi *et al.*, 2022).
416 Lineage tracing further showed that fetal *Wnt5a*$^{+}$ SPs persist and give rise to steroidogenic theca
417 and stromal cells in the ovary as well as FLCs in the testis (Ademi *et al.*, 2022). Thus, while the
418 timing diverges, the overall sequence of SP specification and differentiation is conserved. In testes,
419 newly specified Sertoli cells rapidly trigger SP differentiation into FLCs through DHH and PDGF
420 signalings (Brennan *et al.*, 2003; Clark et al., 2000; Yao et al., 2002). In ovaries, although the SP
421 pool expands during fetal life, SP differentiation is deferred until postnatal folliculogenesis.
422 Consistently, proliferative granulosa cells secrete DHH/IHH from P3 onward, coinciding with
423 *Ptch1* upregulation in SPs (Liu et al., 2015). Together, these findings highlight Hedgehog and
424 PDGF signaling as conserved paracrine pathways that link supporting cells to SPs, synchronizing

425 steroidogenic maturation with gonadal morphogenesis and follicle growth. Yet, key mechanisms
426 remain unresolved, particularly how the ovarian SP pool is balanced over time between
427 maintenance and differentiation into theca cells. The atlas presented here provides a roadmap to
428 reconstruct SP state transitions from fetal priming to postnatal maturation and identifies candidate
429 regulators.
430

431 **A dual origin for granulosa cells**

432 Our study challenges the long-standing view that granulosa cells derive exclusively from the CE
433 and instead supports a convergent, dual-origin model. By combining trajectory inference, lineage
434 tracing, and spatial mapping, we show that granulosa cells arise from two transcriptionally and
435 spatially distinct progenitor pools. CE-derived cells contribute primarily to cortical granulosa cells
436 that maintain the long-term primordial follicle reserve, whereas SLCs give rise to a minor cortical
437 subset and a transient medullar population associated with the first wave of folliculogenesis, largely
438 depleted by puberty. This dual origin adds a new layer of complexity to ovarian lineage architecture
439 and helps reinterpret follicular heterogeneity. Developmental origin likely influences how
440 granulosa subsets interact with oocytes, proliferate, and respond to paracrine and metabolic cues.
441 For example, CE-derived granulosa may be specialized for maintaining oocyte quiescence and
442 orchestrating the maturation of cortical primordial follicles, whereas SLC-derived granulosa may
443 promote rapid activation and growth of medullary follicles. Such functional differences are likely
444 reinforced by microenvironmental differences, including vascularization and signaling niches.
445 Future studies should determine whether CE- and SLC-derived granulosa cells are molecularly and
446 functionally distinct. Comparative transcriptomic and epigenomic profiling could uncover origin-
447 specific signatures, while targeted perturbations could assess redundancy versus complementarity,
448 clarifying whether developmental origin influences folliculogenesis, reproductive lifespan, and
449 overall ovarian functions.
450

451 **Limitations of the study**

452 First, although we show that CE progenitor cells are already heterogeneous and spatially organized
453 in the developing ovary, the molecular signals and transcriptomic programs governing their lineage
454 specification remain largely unknown. Second, because CE-biased progenitors are transient and
455 share markers with their daughter cells, tracing their fate with current lineage-tracing tools remains
456 technically challenging. Third, we relied on *Wnt5a*^{lin} and *Pax8*^{lin} mouse models to describe
457 granulosa cell origins, in which recombinase or rtTA cassettes were inserted by knock-in at the
458 endogenous loci, ensuring expression under the full native regulatory landscape. While no

459 reproductive phenotypes have been reported in the heterozygous females used here, subtle effects
460 of the knock-in cannot be fully excluded. Fourth, while our scRNA-seq dataset provides strong
461 coverage of fetal and early postnatal stages, limited sampling around puberty constraint analysis of
462 transcriptomic dynamics accompanying supporting and steroidogenic lineage differentiation after
463 follicle assembly. In addition, the adult ovarian stroma, including theca cells, steroidogenic stromal
464 cells, and putative steroidogenic progenitors, remains poorly characterized at transcriptomic,
465 spatial, and hormonal levels, warranting deeper investigations. Finally, as this study was conducted
466 in mice, it remains unclear to what extent these developmental processes are conserved in humans
467 and other species. Future analyses using human scRNA-seq and spatial transcriptomics will be
468 essential to determine whether CE heterogeneity, SP specification, and the dual origin of granulosa
469 cells are conserved, with important implications for ovarian pathophysiology.
470

471 **Material & Methods**

472 **Single-cell RNA sequencing analysis**

473 *Data preprocessing*

474 Demultiplexing, alignment, barcode filtering, UMI counting and mapping were performed as
475 described in the original publications: Mayère et al., 2022 (E10.5, E11.5, E12.5, E13.5, E16.5)
476 (Mayere *et al.*, 2022); Niu et Spradling, 2020 (E14.5, E18.5, P1 and P5) (Niu and Spradling, 2020);
477 Rossitto et al., 2022 (P56) (Rossitto et al., 2022). For each sample, to ensure removal of low-quality
478 or empty droplets, barcodes with low UMI counts were removed as described in (Mayere *et al.*,
479 2022). Otherwise, they were removed by visual inspection of the UMI counts density curves.
480 Doublets scores were predicted using Scrublet v0.2.3 (Wolock et al., 2019) via the Scanpy v1.9.8
481 (Wolf et al., 2018) wrapper. Doublet scores thresholds were defined by identifying the closest local
482 minima to the main peak of scores distribution. Barcodes above the thresholds were discarded.
483 Additional quality controls filtering were performed using scanpy.pp.calculate_qc_metrics for
484 mitochondrial and ribosomal content. Cells with >20% mitochondrial counts were removed. XY-
485 contaminating barcodes were identified based on *Ddx3y* expression (discarded if >0). All samples
486 were merged into a single AnnData object, retaining 68,366 cells and 19,961 genes in total: 6,798
487 (E10.5), 5,935 (E11.5), 9,230 (E12.5), 10,866 (E13.5), 9,555 (E14.5), 6,223 (E16.5), 3,186 (E18.5),
488 4,932 (P1), 5,281 (P5), and 6,360 (P56).

489 *Dimensionality reduction and batch correction*

490 Dimensionality reduction and batch correction were performed with scvi.model.SCVI from scVI-
491 tools v1.3.0 (Gayoso et al., 2022) on raw counts data. The model was trained using the samples IDs

492 as batch keys to correct for the batch effects, with the following hyperparameter: 100 latent_space,
493 3 hidden layers with 128 nodes each.
494 *Counts normalization*
495 For expression visualization, differential expression, scoring, and model training, counts were log-
496 normalized. Specifically, for each cell, UMI counts for each gene were divided by the total UMI
497 counts of the cell, multiplied by a factor of 10,000, and log-transformed using
498 scanpy.pp.normalize_total and scanpy.pp.log1p respectively. Cell cycle scoring was performed
499 with scanpy.tl.score_genes_cell_cycle using the gene set from (Tirosh et al., 2016) as input.
500 *Clustering, UMAP embedding, and annotation*
501 For the full atlas, neighbors were computed in the SCVI latent space using scanpy.pp.neighbors
502 with default parameters. Clustering was performed with scanpy.tl.leiden at resolution 1. We used
503 PAGA on subsampled (ncells=200) clusters to optimize the global UMAP topology, we generated
504 and plotted the PAGA graph with default parameters (scanpy.tl.paga) and used PAGA positions as
505 seeds for the UMAP embedding. UMAP embedding was computed with scanpy.tl.umap function
506 with min_dist parameter set to 0.2.
507 scVI based dimensionality reduction and batch correction are highly reliable, at the cost of a
508 substantial loss of temporal information. To account for the time-dependent annotations and avoid
509 inconsistencies, we annotated the dataset at two levels. First, a coarse annotation across the full
510 dataset was performed using known marker expression. Second, refined annotations providing
511 greater accuracy and reducing inconsistencies were carried out at each developmental stage using
512 the coarse annotation as a guide. Each timepoint was clustered and embedded independently using
513 the same preprocessing and clustering pipeline, except that PAGA subsampling was reduced to 100
514 cells per cluster. Known stage-specific markers were used to annotate clusters. Because temporal
515 subsets contain fewer cells, rare cell populations were sometimes difficult to isolate. In ambiguous
516 cases, subclustering was performed with a lower Leiden resolution (0.15 or 0.25). Additionally, the
517 E10.5 subset required a specific annotation strategy due to its lower differentiation state and fraction
518 of gonadal cells: here we retained the coarse annotation and Leiden clustering from the full atlas
519 and defined the mesonephric mesenchyme (MM) population by their low *Gata4* and high *Gata2*
520 expression. Cells from the gonadal domain were subclustered and annotated based on known
521 markers and marker genes specifically expressed in the different compartments at later time points.
522 *Sub-atlases*
523 To focus on the two major somatic lineages of the ovary, we extracted a sub-atlas restricted to
524 ovarian somatic populations. scVI latent space was not recomputed, but the same preprocessing
525 and clustering strategy as in the full atlas was applied. PAGA threshold parameter was set to 0.2,

526 and UMAP min_dist parameter set to 0.3. Additional subsets were generated by isolating ovarian
527 somatic populations at each stage, following the same strategy used for the time-point subsets
528 described above.

529 *Scoring*

530 To create stromal and supporting scores, we trained an ElasticNet model in a one-versus-rest
531 fashion on CE/SE, SLC, stromal (mSP, gSP, PV, SM, Stero) and supporting (preGran, Gran) cells
532 from E12.5 to P5. Model parameters were set to an L1 ratio of 0.5, alpha of 0.01, and tol of 1e-4.
533 To avoid bias from overrepresented cell types, we randomly subsampled each group to match the
534 size of the smallest population prior to training. By comparing each group to the other cells, this
535 approach attributes to each gene a coefficient to create a transcriptomic signature. Genes with high
536 descriptive power are attributed to high coefficients. Consequently, the accuracy of this method
537 depends heavily on the annotation quality and the cellular composition of the subset. For reliability,
538 E10.5 cells were excluded since lineages are not yet committed, and somatic differentiation has not
539 occurred at this stage. We also restricted the analysis to fetal and perinatal data and focused
540 exclusively on ovarian somatic cells (CE/SE, SLC, supporting lineage and steroidogenic/stromal
541 lineage). All the other cell types (adrenosympathetic, erythrocytes, endothelial, germ, immune,
542 mesonephric tubules, mesonephric mesenchyme, perivascular) were excluded from training set.

543 *Differential expression analysis*

544 Differential expression analysis was performed using sc.tl.rank_genes_groups and the Wilcoxon
545 method.

546 **Spatial transcriptomics analysis**

547 *Data collection*

548 The detailed methods to generate the full spatial transcriptome dataset of the developing and adult
549 mouse ovary are reported in (Martinez et al., 2025). Briefly, ovaries from fetal CD-1 outbred mice
550 were collected at E12.5, E14.5 and E16.5, transferred to cryomolds, embedded in OCT, flash frozen
551 and stored at -80ºC. Cryoblocks were sectioned with a Leica cryostat to produce 10µm sections,
552 which were stained with Hematoxylin and Eosin (H&E). H&E-stained slides were imaged at 20x
553 and inspected to choose the highest quality and most representative slide to sequence. Slides were
554 further processed at the University of Colorado Anschutz Medical Campus Genomics Shared
555 resource (RRID: 021984) following the Visium HD Spatial Gene Expression Reagent Kits User
556 Guide (CG000685 Rev B). Sections were hybridized overnight with 10x Genomics' whole
557 transcriptome probe pairs. The prepared slide Visium HD slide were processed on the CytAssist
558 instrument (10x Genomics) for spatial barcoding, followed by library preparation. Libraries were

559 pooled and sequenced on an Illumina NovaSeq X Plus system (150bp x 10bp x 10bp x 150bp),
560 generating approximately 500 million reads per capture area.

561 *Bins annotation*

562 Raw sequencing and imaging data from 10x Visium HD were processed with spaceranger (v3.1.2)
563 as described in (Martinez et al., 2025). Resulting Zarr datasets were then processed with the
564 spatialdata python library. A first bin annotation was performed using a logistic regression model
565 trained on single-cell RNA-seq data, restricted to genes also present in the spatial dataset. To avoid
566 overfitting and bias from over-represented classes, cells were randomly under-sampled with
567 RandomUnderSampler to 100 cells per population. The LogisticRegression model was trained with
568 the following parameters: saga solver, elasticnet regularization (l1_ratio=0.8), a stopping criteria
569 tolerance o= 0.01, and inverse regularization strength = 0.8. The model achieved excellent
570 predictive performance, with an AUC of 1.0 for most cell classes, and 0.99 for CE/SE, SP and SLC.
571 Precision and recall were also high, with the lowest average score observed for SLCs (precisio 0.85)
572 and moSP (recall 0.83).

573 Spatial bins were predicted at 2, 4 and 8µm resolutions using the trained model. Because spatial
574 bins can span multiple cells of different types (e.g. pre-Gran and germ cells), predictions were
575 refined by incorporating spatial context. Specifically, logistic regression prediction scores for each
576 bin were smoothed using those of its eight nearest neighbors. For example, if bin A showed mixed
577 Germ and pre-Gran prediction scores, but its neighbors had strong Germ prediction score, the
578 annotation then Germ score was increased by the score of the neighbors. This was implemented by
579 computing the matrix multiplication between the neighbor connectivities and logistic regression
580 prediction probability matrices. Finally, a predicted confidence threshold was applied to unassign
581 bins with low scores across all classes. This threshold was adapted for each resolution as smaller
582 bins have less transcriptomic content and thus lower overall scores.

583 *Surface epithelium path reconstruction.*

584 Gonadal areas and associated bin were manually annotated in Napari. Each gonad was then aligned
585 using PCA on the spatial coordinates of bins. Since SLCs are the future rete cells and are located is
586 at the antero-posterior pole of the gonads, the averaged SLCs prediction score was used as an
587 orientation cue. Only gonadal sections with a visible junction to the mesonephros were retained for
588 further analysis. CE-associated bins were extracted, and a path along the CE was reconstructed as
589 follows:

590 (1) A spatial neighbor graph of CE-annotated bins was computed using scikit-learn
591 kneighbors_graph on spatial coordinates. To prevent artifacts and unwanted jumps from isolated
592 CE bins or connections between the two CE extremities, long connections were pruned.

593 (1) The shortest paths between all bin pairs were computed with networkx
594 all_pairs_dijkstra_path_length function.
595 (2) Terminal points were defined as the longest geodesic path among the shortest paths.
596 (3) (4) The shortest path between these endpoints was then extracted using networkx shortest path
597 function.
598 (5) All CE bins were projected onto this path using a KD-tree approach: for each CE bins, the
599 nearest path bin was queried, and distances were computed as cumulative sums of distances from
600 root bin in the path.
601 For visualization, bins were ordered along the obtained pseudospace. Because spatial
602 transcriptomic data are sparse, expression values were smoothed with a general additive model
603 (linearGam function of pyGam package), and results were displayed in heatmaps or curves using
604 seaborn.
605 *Scoring of CE and Gene selection for heatmaps*
606 An alternative scoring model was trained on genes detected in both spatial and single-cell RNA-
607 seq datasets. CE bins were then scored with this model. Heatmaps were generated using
608 differentially expressed genes between CE cells of the scRNAseq altas annotated as supporting- or
609 stromal-biased, identified by the ElasticNet model (**Fig. 4C**). Differential expression was assessed
610 with a rank-sum test (log2FC > 1, adj. $p < 0.01$).
611 *Proportion of CE neighbors*
612 For visualization, cell annotations were merged into two lineage categories: Supporting (pre-gran
613 and SLCs) and stromal (gSP, mSP, PV, GM, SM). For each CE bin in each gonad and time point,
614 we calculated the proportion of neighboring cells (k=100) belonging to each lineage. Profiles were
615 then interpolated to normalize path length across gonads and averaged per timepoint for plotting.
616
617 **Transgenic mice and cell lineage tracing**
618 All animal procedure conformed to institutional and European regulations and were approved by
619 the Service de la Consommation et des Affaires Vétérinaires (SCAV) of the Canton de Genève
620 (licenses number GE214-19 and GE35). Animals were maintained on a mixed genetic background
621 under a 12-h light/12-h dark cycle. with ad libitum access to food and water.
622 The alleles used in this study were previously described: *Wnt5atm1(Tet-On 3G)Nef* , *(tetO)7-CMV-*
623 *Cre (TetO:Cre) Pax8tm1.1(cre)Mbu/J* and *Gt(ROSA)26Sortm9(CAG-tdTomato)Hze* (Ademi *et al.*,
624 2022; Bouchard et al., 2002; Madisen et al., 2010; Perl et al., 2002). For constitutive tracing of
625 *Pax8*$^{+}$cells, we generated *Pax8*^{lin} mice (*Pax8tm1.1(cre)Mbu/J*$^{+/ki}$;*Gt(ROSA)26Sortm9(CAG-*
626 *tdTomato)HzeR26RFP/*$^{ki/ki}$). For inducible lineage tracing of *Wnt5a*+ cells, we generated *Wnt5a*^{lin}

627 mice (*Wnt5atm1(Tet-On3G)Nef*$^{+/ki}$*;(tetO)7-CMV-Cre/*$^{+/ki}$*;Gt(ROSA)26Sortm9(CAG-*
628 *tdTomato)HzeR26RFP/*$^{+/ki}$). For *Wnt5a*^{lin}, doxycycline (DOX) was delivered in drinking water (pH
629 6.5) at 2 mg/mL during E11.5-12.5 or E15.5-E16.5. For spatial transcriptome experiments, CD-1
630 outbred mice were housed in an AALAC-accredited barrier facility at the University of Colorado
631 Anschutz Medical campus. All mice were handled and cared for following accepted National
632 Institute of Health guidelines. All experiments were conducted with the approval of the University
633 of Colorado Anschutz Medical Campus Institutional Animal Care and Use Committee (IACUC
634 protocol # 01262). Embryos were staged by detection of a vaginal plug (E0.5), postnatal stages
635 were assigned by day of birth (P0). Ovaries were collected at fetal and adult time points as indicated
636 to follow the fate of *Pax8*+ or *Wnt5a*+ cells across development.
637

638 **Tissue processing, immunofluorescence and in situ hybridization analyses**

639 Embryonic samples were collected at defined stages, fixed in 4% (*w/v*) paraformaldehyde
640 overnight, processed for paraffin embedding, and sectioned into 5 µm sections.
641 Immunofluorescence and Hoechst 33342 (H3570, Invitrogen) staining were performed as described
642 in (Tang et al., 2020) or (Ademi et al., 2022). Primary antibodies included: mouse anti-NR2F2 (PP-
643 H7147-00, R&D, 1/200), rabbit anti-RUNX1 (ab92336, Abcam, 1/500), , rabbit anti-LAMA1
644 (L9303, SIGMA, 1/200), mouse anti-ß-Catenin (BD-610153, BD Biosciences, 1/100), rabbit anti-
645 FOXL2 (1:500, gift from Dagmar Wilhelm, University of Melbourne, Australia), mouse anti-
646 αSMA (1:500, gift from Christine Chaponnier, University of Geneva, Switzerland), rabbit anti-
647 PAX8 (1:500, 10336-1-AP, Proteintech), mouse anti-RFP (DsRed) (1:250, sc-390909, SantaCruz
648 Biotechnology, USA), goat anti-RFP (1:50, 200-101-379, Rockland Immunochemicals Inc., USA),
649 rabbit anti-RFP (1:250, 600-401-379, Rockland Immunochemicals Inc., USA) and rabbit anti-
650 CYP11A1 (1:500, gift from Dagmar Wilhelm, University of Melbourne, Australia).

651 RNAscope in situ hybridization was performed using the RNAscope Multiplex Fluorescent
652 Reagent Kit v2 (Advanced Cell Diagnostic) using probes for *Bmp2* (406661-C3) and *Upk3b*
653 (568561) following the manufacturer's instructions.
654 Fluorescent images were acquired on Axio Imager M2 or Z1 microscope (ZEISS, Germany)
655 equipped with Axiocam 702 mono camera or MRm camera (ZEISS, Germany), and or on a Zeiss
656 LSM 780 confocal microscope with a 40x/1.2 W objective. Images were minimally adjusted for
657 global levels in ZEN (ZEISS), processed in Fiji (Bethesda, MD, USA) and assembled using
658 OMERO (https://www.openmicroscopy.org/omero/).
659

660 **Immunofluorescence quantification and statistical analysis**

661 Cell quantifications were performed using QuPath-0.5.1. Nuclei were detected by DAPI intensity,
662 cells were classified as positive/negative based on mean signal intensity thresholds for FOXL2 or
663 tdTomato (thresholds set per experiment). For each condition, 3-5 biological replicates (whole-
664 ovary sections) were analyzed. Results are reported as percentage of tdTomato+ cells (Mean ± SD).
665 Statistical analyses were performed in GraphPad Prism (version 10). Pairwise comparisons used
666 two-tailed Mann-Whitney U tests. Significance was defined as $P < 0.05$. n biological replicates and
667 statistical details are provided in Figure legends.

668

669 **Additional resources**

670 An interactive viewer is available for further exploration
671 [https://www.unige.ch/medecine/nef/datasets].

672

673 **Acknowledgments:**

674 We thank Karim Hammad, Coralie Gobbo, Françoise Kuhne, Violette Regard and Jean-Luc Pitetti
675 for their assistance with animal handling, genotyping, and immunofluorescence experiments. We
676 are grateful to Nicolas Liaudet for support with the Bioimaging platform and to the animal facility
677 team at the Faculty of Medicine, University of Geneva, for their technical assistance. We are also
678 grateful to the members of the Nef laboratory for valuable discussions and critical reading of the
679 manuscript.

680

681 **Funding**

682 This work was supported by the Département de l'Instruction Publique of the State of Geneva and
683 by Swiss National Science Foundation grants (31003A_173070, 310030_200316 and 10.001.251)
684 awarded to S.N. MCC was supported by the Agence nationale de la recherche (ANR, France)
685 through grants ANR-23-CE14-0012 (HeteroSex) and ANR-24-CE14-2476 (Anaform). JM was
686 supported by National Institutes of Health grant #R00HD103778 and by funding from CU Anschutz
687 Medical Campus, Department of Pediatrics.

688

689 **Author Contributions**

690 CD, CM, and SN conceived and designed the study. CD, PB, APG, AR, CG, HA, and DW
691 performed mouse experiments, lineage tracing, immunofluorescence, and other analyses. AM and
692 TG generated spatial transcriptomic data. CM and MG conducted bioinformatics analyses. CD,

CM, MG, and SN drafted the manuscript. All authors contributed to manuscript revision and approved the final version. Funding and resources: SN, MCC, JM, DW. Supervision: SN.

Competing Interests

The authors declare no competing interests.

Data and materials availability

All data needed to evaluate the paper are present in the paper and/or the Supplementary Materials. The scRNAseq datasets are available at NCBI Gene Expression Omnibus GEO: GSE184708.

References

Ademi, H., Djari, C., Mayere, C., Neirijnck, Y., Sararols, P., Rands, C.M., Stevant, I., Conne, B., and Nef, S. (2022). Deciphering the origins and fates of steroidogenic lineages in the mouse testis. Cell Rep *39*, 110935.

Barsoum, I.B., and Yao, H.H. (2010). Fetal Leydig cells: progenitor cell maintenance and differentiation. J Androl *31*, 11-15.

Bouchard, M., Souabni, A., Mandler, M., Neubuser, A., and Busslinger, M. (2002). Nephric lineage specification by Pax2 and Pax8. Genes Dev *16*, 2958-2970.

Brennan, J., Tilmann, C., and Capel, B. (2003). Pdgfr-alpha mediates testis cord organization and fetal Leydig cell development in the XY gonad. Genes Dev *17*, 800-810.

Bunce, C., Barske, L., Zhang, G., and Capel, B. (2023). Biased precursor ingression underlies the center-to-pole pattern of male sex determination in mouse. Development *150*.

Cai, H., Liu, B., Wang, H., Sun, G., Feng, L., Chen, Z., Zhou, J., Zhang, J., Zhang, T., He, M.*, et al.* (2020). SP1 governs primordial folliculogenesis by regulating pregranulosa cell development in mice. J Mol Cell Biol *12*, 230-244.

Capel, B. (2000). The battle of the sexes. Mech Dev *92*, 89-103.

Clark, A.M., Garland, K.K., and Russell, L.D. (2000). Desert hedgehog (Dhh) gene is required in the mouse testis for formation of adult-type Leydig cells and normal development of peritubular cells and seminiferous tubules. Biol Reprod *63*, 1825-1838.

Cowan, R.G., and Quirk, S.M. (2021). Cells responding to hedgehog signaling contribute to the theca of ovarian follicles. Reproduction *161*, 437-448.

Cui, S., Ross, A., Stallings, N., Parker, K.L., Capel, B., and Quaggin, S.E. (2004). Disrupted gonadogenesis and male-to-female sex reversal in Pod1 knockout mice. Development *131*, 4095-4105.

DeFalco, T., Takahashi, S., and Capel, B. (2011). Two distinct origins for Leydig cell progenitors in the fetal testis. Dev Biol *352*, 14-26.

Eliveld, J., van den Berg, E.A., Chikhovskaya, J.V., van Daalen, S.K.M., de Winter-Korver, C.M., van der Veen, F., Repping, S., Teerds, K., and van Pelt, A.M.M. (2019). Primary human testicular PDGFRalpha+ cells are multipotent and can be differentiated into cells with Leydig cell characteristics in vitro. Hum Reprod *34*, 1621-1631.

Estermann, M.A., Grimm, S.A., Kitakule, A.S., Rodriguez, K.F., Brown, P.R., McClelland, K., Amato, C.M., and Yao, H.H. (2025). NR2F2 regulation of interstitial cell fate in the embryonic mouse testis and its impact on differences of sex development. Nat Commun *16*, 3987.

Feng, L., Wang, Y., Cai, H., Sun, G., Niu, W., Xin, Q., Tang, X., Zhang, J., Wang, C., Zhang, H.*, et al.* (2016). ADAM10-Notch signaling governs the recruitment of ovarian pregranulosa cells and controls folliculogenesis in mice. J Cell Sci *129*, 2202-2212.

Fortune, J.E., and Armstrong, D.T. (1977). Androgen production by theca and granulosa isolated from proestrous rat follicles. Endocrinology *100*, 1341-1347.

Garcia-Alonso, L., Lorenzi, V., Mazzeo, C.I., Alves-Lopes, J.P., Roberts, K., Sancho-Serra, C., Engelbert, J., Marečková, M., Gruhn, W.H., Botting, R.A.*, et al.* (2022). Single-cell roadmap of human gonadal development. Nature *607*, 540-547.

Gayoso, A., Lopez, R., Xing, G., Boyeau, P., Valiollah Pour Amiri, V., Hong, J., Wu, K., Jayasuriya, M., Mehlman, E., Langevin, M.*, et al.* (2022). A Python library for probabilistic analysis of single-cell omics data. Nature Biotechnology *40*, 163-166.

Ge, R.S., Dong, Q., Sottas, C.M., Papadopoulos, V., Zirkin, B.R., and Hardy, M.P. (2006). In search of rat stem Leydig cells: identification, isolation, and lineage-specific development. Proc Natl Acad Sci U S A *103*, 2719-2724.

Gong, S., Zheng, C., Doughty, M.L., Losos, K., Didkovsky, N., Schambra, U.B., Nowak, N.J., Joyner, A., Leblanc, G., Hatten, M.E.*, et al.* (2003). A gene expression atlas of the central nervous system based on bacterial artificial chromosomes. Nature *425*, 917-925.

753 Gustin, S.E., Hogg, K., Stringer, J.M., Rastetter, R.H., Pelosi, E., Miles, D.C., Sinclair, A.H.,
754 Wilhelm, D., and Western, P.S. (2016). WNT/beta-catenin and p27/FOXL2 differentially regulate
755 supporting cell proliferation in the developing ovary. Dev Biol *412*, 250-260.
756 Karl, J., and Capel, B. (1998). Sertoli cells of the mouse testis originate from the coelomic
757 epithelium. Developmental Biology *203*, 323-333.
758 Kilcoyne, K.R., Smith, L.B., Atanassova, N., Macpherson, S., McKinnell, C., van den Driesche, S.,
759 Jobling, M.S., Chambers, T.J., De Gendt, K., Verhoeven, G.*, et al.* (2014). Fetal programming of
760 adult Leydig cell function by androgenic effects on stem/progenitor cells. Proc Natl Acad Sci U S
761 A *111*, E1924-1932.
762 Kumar, D.L., and DeFalco, T. (2018). A perivascular niche for multipotent progenitors in the fetal
763 testis. Nat Commun *9*, 4519.
764 Kusaka, M., Katoh-Fukui, Y., Ogawa, H., Miyabayashi, K., Baba, T., Shima, Y., Sugiyama, N.,
765 Sugimoto, Y., Okuno, Y., Kodama, R.*, et al.* (2010). Abnormal epithelial cell polarity and ectopic
766 epidermal growth factor receptor (EGFR) expression induced in Emx2 KO embryonic gonads.
767 Endocrinology *151*, 5893-5904.
768 Lin, Y.T., Barske, L., DeFalco, T., and Capel, B. (2017). Numb regulates somatic cell lineage
769 commitment during early gonadogenesis in mice. Development *144*, 1607-1618.
770 Liu, C., Peng, J., Matzuk, M.M., and Yao, H.H. (2015). Lineage specification of ovarian theca cells
771 requires multicellular interactions via oocyte and granulosa cells. Nat Commun *6*, 6934.
772 Liu, C., Rodriguez, K., and Yao, H.H. (2016). Mapping lineage progression of somatic progenitor
773 cells in the mouse fetal testis. Development *143*, 3700-3710.
774 Madisen, L., Zwingman, T.A., Sunkin, S.M., Oh, S.W., Zariwala, H.A., Gu, H., Ng, L.L., Palmiter,
775 R.D., Hawrylycz, M.J., Jones, A.R.*, et al.* (2010). A robust and high-throughput Cre reporting and
776 characterization system for the whole mouse brain. Nat Neurosci *13*, 133-140.
777 Magoffin, D.A. (2005). Ovarian theca cell. Int J Biochem Cell Biol *37*, 1344-1349.
778 Magoffin, D.A., and Weitsman, S.R. (1994). Insulin-like growth factor-I regulation of luteinizing
779 hormone (LH) receptor messenger ribonucleic acid expression and LH-stimulated signal
780 transduction in rat ovarian theca-interstitial cells. Biol Reprod *51*, 766-775.
781 Mannan, M.A., and O'Shaughnessy, P.J. (1991). Steroidogenesis during postnatal development in
782 the mouse ovary. J Endocrinol *130*, 101-106.
783 Martinez, A.S., Gibson, T.J., and McKey, J. (2025). Single-cell-scale spatial transcriptome of the
784 developing and adult mouse ovary. bioRxiv, 2025.2009.2016.676655.
785 Mayere, C., Regard, V., Perea-Gomez, A., Bunce, C., Neirijnck, Y., Djari, C., Bellido-Carreras, N.,
786 Sararols, P., Reeves, R., Greenaway, S.*, et al.* (2022). Origin, specification and differentiation of a
787 rare supporting-like lineage in the developing mouse gonad. Sci Adv *8*, eabm0972.
788 McKey, J., Anbarci, D.N., Bunce, C., Ontiveros, A.E., Behringer, R.R., and Capel, B. (2022).
789 Integration of mouse ovary morphogenesis with developmental dynamics of the oviduct, ovarian
790 ligaments, and rete ovarii. Elife *11*.
791 Miyabayashi, K., Katoh-Fukui, Y., Ogawa, H., Baba, T., Shima, Y., Sugiyama, N., Kitamura, K.,
792 and Morohashi, K. (2013). Aristaless related homeobox gene, Arx, is implicated in mouse fetal
793 Leydig cell differentiation possibly through expressing in the progenitor cells. PLoS ONE *8*,
794 e68050.
795 Mork, L., Maatouk, D.M., McMahon, J.A., Guo, J.J., Zhang, P., McMahon, A.P., and Capel, B.
796 (2012). Temporal differences in granulosa cell specification in the ovary reflect distinct follicle
797 fates in mice. Biol Reprod *86*, 37.
798 Neirijnck, Y., Sararols, P., Kühne, F., Mayère, C., Weerasinghe Arachchige, L.C., Regard, V., Nef,
799 S., and Schedl, A. (2023). Single-cell transcriptomic profiling redefines the origin and specification
800 of early adrenogonadal progenitors. Cell Rep *42*, 112191.
801 Nicol, B., Estermann, M.A., Yao, H.H., and Mellouk, N. (2022). Becoming female: Ovarian
802 differentiation from an evolutionary perspective. Front Cell Dev Biol *10*, 944776.

803 Niu, W., and Spradling, A.C. (2020). Two distinct pathways of pregranulosa cell differentiation
804 support follicle formation in the mouse ovary. Proc Natl Acad Sci U S A *117*, 20015-20026.
805 Perea-Gomez, A., Bellido Carreras, N., Dhellemmes, M., Tang, F., Le Gallo, C., and Chaboissier,
806 M.C. (2025). NR2F2 is required in the embryonic testis for fetal Leydig cell development. Elife *14*.
807 Perl, A.K., Wert, S.E., Nagy, A., Lobe, C.G., and Whitsett, J.A. (2002). Early restriction of
808 peripheral and proximal cell lineages during formation of the lung. Proc Natl Acad Sci U S A *99*,
809 10482-10487.
810 Qin, J., Tsai, M.J., and Tsai, S.Y. (2008). Essential roles of COUP-TFII in Leydig cell
811 differentiation and male fertility. PLoS ONE *3*, e3285.
812 Qiu, C., Martin, B.K., Welsh, I.C., Daza, R.M., Le, T.M., Huang, X., Nichols, E.K., Taylor, M.L.,
813 Fulton, O., O'Day, D.R.*, et al.* (2024). A single-cell time-lapse of mouse prenatal development from
814 gastrula to birth. Nature *626*, 1084-1093.
815 Rastetter, R.H., Bernard, P., Palmer, J.S., Chassot, A.A., Chen, H., Western, P.S., Ramsay, R.G.,
816 Chaboissier, M.C., and Wilhelm, D. (2014). Marker genes identify three somatic cell types in the
817 fetal mouse ovary. Dev Biol *394*, 242-252.
818 Richards, J.S., Ren, Y.A., Candelaria, N., Adams, J.E., and Rajkovic, A. (2017). Ovarian Follicular
819 Theca Cell Recruitment, Differentiation, and Impact on Fertility: 2017 Update. Endocrine Reviews
820 *39*, 1-20.
821 Rossitto, M., Déjardin, S., Rands, C.M., Le Gras, S., Migale, R., Rafiee, M.R., Neirijnck, Y.,
822 Pruvost, A., Nguyen, A.L., Bossis, G.*, et al.* (2022). TRIM28-dependent SUMOylation protects the
823 adult ovary from activation of the testicular pathway. Nat Commun *13*, 4412.
824 Rotgers, E., Jorgensen, A., and Yao, H.H. (2018). At the Crossroads of Fate-Somatic Cell Lineage
825 Specification in the Fetal Gonad. Endocr Rev *39*, 739-759.
826 Schmahl, J., and Capel, B. (2003). Cell proliferation is necessary for the determination of male fate
827 in the gonad. Dev Biol *258*, 264-276.
828 Schmahl, J., Eicher, E.M., Washburn, L.L., and Capel, B. (2000). Sry induces cell proliferation in
829 the mouse gonad. Development *127*, 65-73.
830 Schmahl, J., Yao, H.H., Pierucci-Alves, F., and Capel, B. (2003). Colocalization of WT1 and cell
831 proliferation reveals conserved mechanisms in temperature-dependent sex determination. Genesis
832 *35*, 193-201.
833 Shen, Y.C., Shami, A.N., Moritz, L., Larose, H., Manske, G.L., Ma, Q., Zheng, X., Sukhwani, M.,
834 Czerwinski, M., Sultan, C.*, et al.* (2021). TCF21(+) mesenchymal cells contribute to testis somatic
835 cell development, homeostasis, and regeneration in mice. Nat Commun *12*, 3876.
836 Stevant, I., Kuhne, F., Greenfield, A., Chaboissier, M.C., Dermitzakis, E.T., and Nef, S. (2019).
837 Dissecting Cell Lineage Specification and Sex Fate Determination in Gonadal Somatic Cells Using
838 Single-Cell Transcriptomics. Cell Rep *26*, 3272-3283 e3273.
839 Stevant, I., and Nef, S. (2018). Single cell transcriptome sequencing: A new approach for the study
840 of mammalian sex determination. Mol Cell Endocrinol *468*, 11-18.
841 Stevant, I., and Nef, S. (2019). Genetic Control of Gonadal Sex Determination and Development.
842 Trends Genet *35*, 346-358.
843 Tang, F., Richardson, N., Albina, A., Chaboissier, M.C., and Perea-Gomez, A. (2020). Mouse
844 Gonad Development in the Absence of the Pro-Ovary Factor WNT4 and the Pro-Testis Factor
845 SOX9. Cells *9*.
846 Tirosh, I., Izar, B., Prakadan, S.M., Wadsworth, M.H., 2nd, Treacy, D., Trombetta, J.J., Rotem, A.,
847 Rodman, C., Lian, C., Murphy, G.*, et al.* (2016). Dissecting the multicellular ecosystem of
848 metastatic melanoma by single-cell RNA-seq. Science *352*, 189-196.
849 Wilhelm, D., Yang, J.X., and Thomas, P. (2013). Chapter Three - Mammalian Sex Determination
850 and Gonad Development. In Current Topics in Developmental Biology, P. Thomas, ed. (Academic
851 Press), pp. 89-121.

852 Wolf, F.A., Angerer, P., and Theis, F.J. (2018). SCANPY: large-scale single-cell gene expression
853 data analysis. Genome Biol *19*, 15.
854 Wolock, S.L., Lopez, R., and Klein, A.M. (2019). Scrublet: Computational Identification of Cell
855 Doublets in Single-Cell Transcriptomic Data. Cell Syst *8*, 281-291 e289.
856 Yao, H.H., Whoriskey, W., and Capel, B. (2002). Desert Hedgehog/Patched 1 signaling specifies
857 fetal Leydig cell fate in testis organogenesis. Genes Dev *16*, 1433-1440.
858 Zheng, W., Zhang, H., Gorre, N., Risal, S., Shen, Y., and Liu, K. (2014). Two classes of ovarian
859 primordial follicles exhibit distinct developmental dynamics and physiological functions. Hum Mol
860 Genet *23*, 920-928.
861

862 **Figure legends**

863 **Figure 1. Single cell transcriptomic atlas of developing mouse ovaries.**

864 (A) Schematic overview of ovarian development and study design. Single-cell RNA-seq data were
865 combined from three published datasets (Mayère et al., 2022; Niu and Spradling, 2020; Rossitto et
866 al., 2022), spanning 10 developmental stages (E10.5, E11.5, E12.5, E13.5, E14.5, E16.5, E18.5,
867 P1, P5, P56).

868 (B) Barplot of cell numbers per developmental stage, subdivided by single cell captures and color-
869 coded by dataset source.

870 (C-E) UMAP of 68,366 cells, colored by (C) dataset source, (D) developmental stage, and (E)
871 annotated cell type.

872 (F) Dotplot of marker gene expression across annotated cell populations. Dot size indicates the
873 percentage of expressing cells; color indicates average normalized expression (per-gene scaled).
874 Marker genes for each cell type are highlighted in blue.

875 (G and H) Conductance-based Partition-based Graph Abstraction (cPAGA) showing connectivity
876 between cell populations in the ovarian somatic subset (G) and at each developmental stage (H).
877 Edge width reflects the conductance score.

878 (I and J) UMAP of the 42,199 ovarian somatic cells colored by developmental stage (I) and
879 annotated cell types (J). Arrows represent hypothetical trajectories.

880 (K) Cell proportion of ovarian somatic cells from E10.5 to P56.

881 (L) Somatic cell proliferation indicated as a percentage of cells in G2/M phase by compartment
882 across stages. Supporting includes pre-Sup, pre-Gran and Gran; Stromal includes GM, gSP, Stero,
883 SM and PV.

884 Cell type abbreviation: CE, coelomic epithelium; SE, surface epithelium cells; pre-Sup, pre-
885 supporting cells; pre-Gran, pre-granulosa cells; Gran, granulosa cells; SLC, supporting-like cells;
886 GM, gonadal mesenchyme; gSP, gonadal stromal progenitors; Stero, steroidogenic cells; SM,
887 smooth muscle cells; PV, perivascular cells; MT, mesonephric tubules; MM, mesonephric
888 mesenchyme; mSP, mesonephric stromal progenitors; AS, adrenosympathetic cells; End,
889 endothelial cells; Eryt, erythrocytes.

890

891 **Figure 2. Dual origins of pre-granulosa cell revealed by *in vivo* lineage tracing.**

892 (A) UMAP of ovarian somatic cells colored by cell type, highlighting CE/SE, SLC and Gran. The
893 hypothetical trajectory from CE/SE cells towards Gran is indicated.

894 (B) Mean *Wnt5a* expression across ovarian somatic compartments (CE, SLC, Supporting and
895 Stromal lineages) from E10.5 to P56.
896 (C and D) UMAPs highlighting ovarian somatic cells at E11.5 and E12.5 (C) and *Wnt5a* expression
897 (D).
898 (E) Schematic of the *Wnt5a*^{lin} mouse model (*Wnt5-rtTA;TetO-Cre;R26-tdTomato*). Upon DOX
899 exposure, Tet-On3G induces Cre expression, excising the STOP cassette in the R26-LSL-
900 *tdTomato* locus and resulting in permanent tdTomato labeling of *Wnt5a*$^{+}$ cells.
901 (F) *In vivo* lineage-tracing design. Pregnant females were exposed to DOX between E11.5 and
902 E12.5 and ovaries were collected at E12.5, E16.5, P5, and 8 weeks.
903 (G) Co-IF for tdTomato and the pre-granulosa marker FOXL2 in *Wnt5a*^{lin} ovaries at E12.5 and E16.
904 (H) Quantification of tdTomato^{+} as a percentage of total FOXL2^{+} pre-granulosa cells at E12.5 and
905 E16.5.
906 (I) Co-IF for tdTomato and FOXL2 in *Wnt5a*^{lin} ovaries at P5 and 8 weeks.
907 (J) Quantification of tdTomato^{+} as a percentage of total FOXL2^{+} pre-granulosa cells at 8 weeks.
908 (K) UMAP of ovarian somatic cells colored by cell type, with the hypothetical trajectory from SLCs
909 towards granulosa cells (Gran) highlighted.
910 (L) Mean *Pax8* expression across ovarian somatic compartments (CE, SLC, Sup., Stromal) from
911 E10.5 to P56.
912 (M and N) UMAP of ovarian somatic cells colored by developmental stages (M) and *Pax8*
913 expression highlighted in the CE/SE, SLC, Sup cell populations (N).
914 (O) Schematic of the constitutive *Pax8*^{lin} mouse model (*Pax8:Cre;R26-tdTomato*). *Pax8:Cre*
915 knock-in drives *Cre* expression under the control of *Pax8* endogenous promoter. Cre-mediated
916 excision of the STOP cassette at the R26-LSL-tdTomato locus permanently labeled tdTomato
917 *Pax8*$^{+}$ cells and their daughter cells.
918 (P) *In vivo* lineage-tracing design. Ovaries were collected at E12.5, E16.5, P5, and 8 weeks.
919 (Q) Co-IF for tdTomato and FOXL2 in *Pax8*^{lin} ovaries at E12.5 and E16.5.
920 (R) Quantification of tdTomato^{+} as a percentage of total FOXL2^{+} pre-granulosa cells at E12.5 and
921 E16.5.
922 (S) Co-IF for tdTomato and FOXL2 in *Pax8*^{lin} ovaries at P5 and 8 weeks.
923 (T) Quantification of tdTomato^{+} as a percentage of total FOXL2^{+} pre-granulosa at 8 weeks.
924 Arrowheads indicate double-positive cells. Dashed lines delineate CE/SE. Scale bars, 100 μm.
925 Error bars represent mean ± SD.
926

927 **Figure 3. The coelomic epithelium is transcriptionally heterogeneous and biased towards a**
928 **supporting or stromal identity.**
929 (A) UMAP of the 42,199 ovarian somatic cells, colored by annotated cell types, with trajectories
930 from CE cells toward supporting and steroidogenic lineages.
931 (B) UMAPs showing expression of *Upk3b* (CE/SE marker), *Wnt6* (Sup marker) and *Tcf21* (gSP
932 marker).
933 (C) UMAPs of supporting (pre-Sup, pre-Gran, Gran) and stromal identity (gSP, mSP, Stero, PV
934 and SM) scores. Color scales are clipped at the 1st and 99th percentiles to enhance visualization
935 and minimize outliers' impact.
936 (D) UMAP of fate bias within CE/SE cells classified as stromal-biased if stromal score > supporting
937 score, or supporting-biased otherwise.
938 (E) Venn diagram comparing differentially expressed genes (DEG) between supporting versus
939 stromal cells and between sup-biased versus stromal-biased CE/SE subsets (l adj. $p < 0.05$).
940 (F) Scatterplot of sSupporting and stromal scores per CE/SE cell across stages (E11.5-P5).
941 (G) Lineplot of median supporting and stromal identity scores with 95% confidence intervals across
942 stages.
943 (H) Heatmap of the percentage of CE/SE cells expressing supporting markers (*Bmp2, Irx3, Lgr5,*
944 *Runx1* and *Wnt6*) and gSP markers (*Arx*, *Nr2f2, Pdfgra* and *Tcf21*) across stages, ordered by
945 transcriptomic progression (E11.5-P5).
946 (I) Heatmap of conductance scores quantifying connectivity between CE/SE and stromal or
947 supporting cells across stages. Cell type abbreviation: CE/SE, coelomic/surface epithelium cells;
948 pre-Sup, pre-supporting cells; pre-Gran, pre-granulosa cells; Gran, granulosa cells; gSP, gonadal
949 stromal progenitors; Stero, steroidogenic cells, SM, smooth muscle cells; PV, perivascular cells.
950
951
952 **Figure 4. Primed-ceolomic epithelium cells are dynamically and spatially resolved.**
953 (A) Spatial transcriptomic experimental design using 10x Visium HD technology on parasagittal
954 ovaries/mesonephros sections. Gonads and CE were annotated, CE paths were reconstructed and
955 gene expression/score computed along a pseudospace.
956 (B) Lineplots of smoothed stromal- and supporting- identity scores along CE pseudospace at E12.5,
957 E14.5 and E16.5 (Mean with 95% confidence intervals).
958 (C) Heatmap of gene expression along CE pseudospace at E12.5 for differentially expressed genes
959 between supporting-biased (n=340) and stromal-biased (n=273) CE subsets from the scRNA-seq
960 atlas (log2FC > 1, adj. $p < 0.01$). Genes are ordered by pattern similarity.

(D) Lineplots of smoothed *Bmp2* and *Nr2f2* expression along CE pseudospace at E12.5, E14.5 and E16.5 (Mean with 95% confidence intervals).

(E and F) Combined ISH/IF for *Upk3b* (CE/SE), *Bmp2 (*supporting*)* and NR2F2 (steroidogenic) (E) or β-catenin and LAMA1 (F) on developing ovaries at E12.5, E13.5 and E16.5. White dashed lines: CE, green dashed: intragonadal region enriched in NR2F2+ cells; magenta dashed lines: intragonadal region enriched in *Bmp2*$^{+}$ cells. Arrowheads indicate basal lamina discontinuities.

(G) Stacked-area plots showing the proportion of intragonadal neighbors (pre-granulosa+SLCs, Stromal Progenitors (gSP) and germ cells) among the 100 nearest spatial neighbors of CE bins along pseudospace.

(H) *In vivo* lineage-tracing design. Pregnant *Wnt5a*^{lin} females were exposed to DOX between E15.5-E16.5 when *Wnt5a* expression is restricted to SPs. Ovaries were collected at E16.5 and 8 weeks.

(I) Co-IF for tdTomato and NR2F2 in *Wnt5a*^{lin} ovaries at E16.5. Arrowheads: double-positive cells.

(J) Co-IF for tdTomato with FOXL2, NR2F2 (stromal cells), or CYP11A1 (steroidogenic cells) in *Wnt5a*^{lin} ovaries at 8 weeks. Yellow lines: follicular granulosa cells; yellow dashed lines: thecal compartment. Scale bars, 100μm. Cell type abbreviation: CE/SE, coelomic/surface epithelium cells; pre-Gran, pre-granulosa cells; Gran, granulosa cells; gSP, gonadal stromal progenitors.

Figure 5. Model for ovarian development in mammals.

CE cells covering the fetal mouse ovary are transcriptionally heterogeneous and spatially organized, with subsets primed toward supporting or steroidogenic fates whose transcriptomes resemble their respective target lineages. Steroidogenic-primed CE cells express canonic SP markers (*Arx*, *Nr2f2, Pdfgra and Tcf21*), while supporting-primed CE cells express canonical supporting markers (*Bmp2, Irx3, Lgr5, Runx1,* and *Wnt6*). From E11.5-E12.5 onward, stromal-primed CE cells localize near the gonad–mesonephros junction, while supporting-primed CE cells occupy the central surface. After E14.5, stromal-primed CE cells decline sharply, and by E16.5 CE cells are almost exclusively supporting-biased. Granulosa cells arise through a convergent process from two transcriptionally distinct progenitors: CE and SLCs. CE-derived granulosa cells form the cortical granulosa population maintains the primordial follicle reserve, whereas SLC-derived granulosa cells contribute to a minor cortical subset and a transient medullary subset associated with the first follicle wave, largely depleted by puberty. During a restricted fetal window (E11.5–E14.5), a subset of CE progenitors acquires a steroidogenic bias and gives rise to intraovarian SPs. SPs proliferate extensively, expand to ~41% of ovarian cells by P5, and persist to adulthood. SPs give rise to

994 steroidogenic theca and stromal cells in the ovary. Cell type abbreviation: SLC, supporting-like
995 cells. Abbreviations to complete
996
997 **Supplementary Figure S1 related to Figure 1. Annotation of the single-cell transcriptomic**
998 **atlas of developing mouse ovaries.**
999 (A-C) UMAPs of each developmental stages (E10.5 to P65) colored by sample IDs (A), Leiden
1000 clustering (B), and annotation (C). For E10.5, clustering was performed in two steps: non-gonadal
1001 cells (clusters associated to green number) were annotated from the complete atlas, in blue, gonadal
1002 cells (clusters associated to blue number) were re-clustered from a stage specific subset to refine
1003 annotation.
1004 (D) Dotplots showing expression of known markers across Leiden clusters. Dot size represents the
1005 percentage of cells and color represents mean expression normalized by cluster. Abbreviations:
1006 Cell type abbreviation: SE, surface epithelium cells; preSup, pre-supporting cells; preGran, pre-
1007 granulosa cells; Gran, granulosa cells; SLC, supporting-like cells; GM, gonadal mesenchyme; gSP,
1008 gonadal stromal progenitors; Stero, steroidogenic cells; SM, smooth muscle cells; PV, perivascular
1009 cells; Luteal, luteal cells; Germ, germinal cells; MT, mesonephric tubules; MM, mesonephric
1010 mesenchyme; mSP, mesonephric stromal progenitors; AS, adreno
1011 sympatic cells; End, endothelial cells; Eryt, erythrocytes; Imm, immune cells.
1012
1013 **Supplementary Figure S2 related to Figure 2.**
1014 (A) Co-IF for GATA4 and PAX8 in E12.5 and E16.5 fetal ovaries. White line: ovarian domain,
1015 dashed line: mesonephric domain.
1016 (B) IF for PAX8 in P0, P10 and adult *Pax8*^{lin} ovaries showing PAX8 expression restricted to the
1017 rete ovarii.
1018 (C) IF for tdTomato in P5 *Pax8*^{lin} ovaries. Blue line: Rete ovarii, white line: cortical compartment,
1019 yellow dashed line: medullar compartment.
1020 (D) Quantification of tdTomato^{+} as a percentage of total FOXL2^{+} pre-granulosa cells in the cortical
1021 and medullar ovarian compartments at P5. Scale bars, 100 µm. Error bars represent mean ± SD.
1022
1023 **Supplementary Figure S3 related to Figure 3.**
1024 UMAPs showing expression of supporting markers (*Bmp2*, *Irx3*, *Lgr5* and *Runx1*) and
1025 steroidogenic progenitor markers (*Arx*, *Nr2f2* and *Pfgra*) in the ovarian somatic subset.
1026
1027 **Supplementary Figure S4 related to Figure 4.**

1028 (A) Heatmaps of gene expression varying along CE pseudospace at E14.5 and E16.5 for
1029 differentially expressed genes between supporting-biased (n=340) and stromal-biased (n=273) CE
1030 subsets from the scRNA-seq atlas (log2FC > 1, adj. $p < 0.01$). Genes are ordered by pattern
1031 similarity.
1032 (B) Smoothed *Runx1* and *Tcf21* expression along CE pseudospace at E14.5 and E16.5 (Mean with
1033 95% confidence intervals).
1034 (C) Combined IF for RUNX1 (supporting) and NR2F2 (F) on developing ovaries at E12.5, E13.5
1035 and E16.5. White dashed lines: CE. (D and E) Combined ISH/IF on XX gonads at E11.5 for (D)
1036 *Upk3b* (CE/SE), *Bmp2 (supporting)* and NR2F2 (steroidogenic) or (E) RUNX1 (supporting) and
1037 NR2F2. White dashed lines, white solid line: interface between NR2F2-enriched domain and the
1038 *Bmp2*-enriched domains. Insets are color-bordered based local enrichment (green: NR2F2-
1039 enriched, magenta: *Bmp2*-enriched).
1040
1041
1042
1043

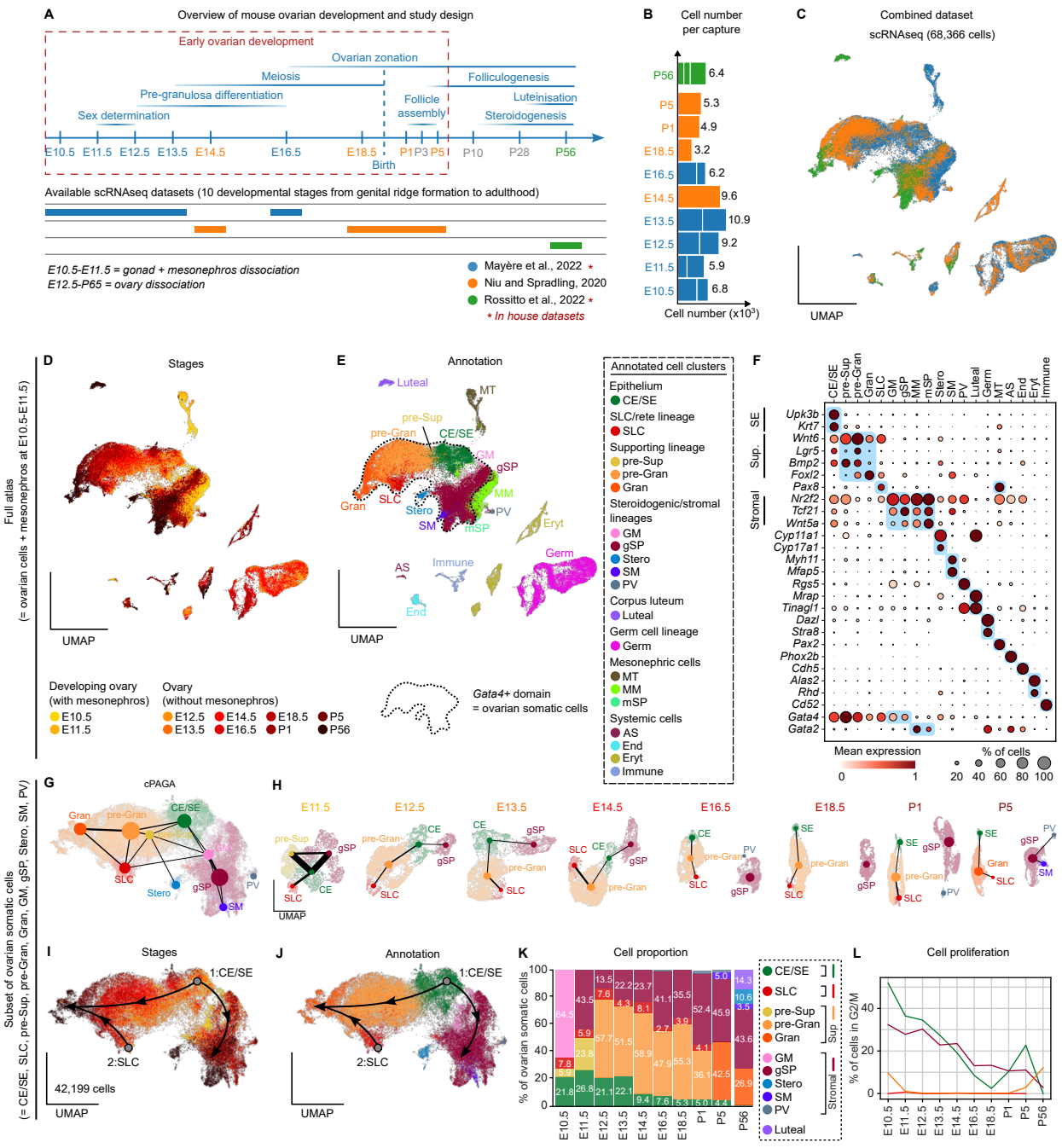
A
Overview of mouse ovarian development and study design
Early ovarian development
Ovarian zonation
Meiosis
Folliculogenesis
Pre-granulosa differentiation
Luteinisation
Follicle assembly
Sex determination
Steroidogenesis
E10.5 E11.5 E12.5 E13.5 E14.5 E16.5 E18.5 P1 P3 P5 P10 P28 P56
Birth
Available scRNAseq datasets (10 developmental stages from genital ridge formation to adulthood)
E10.5-E11.5 = gonad + mesonephros dissociation
E12.5-P65 = ovary dissociation
Mayère et al., 2022 *
Niu and Spradling, 2020
Rossitto et al., 2022 *
* In house datasets
B
Cell number per capture
P56 6.4
P5 5.3
P1 4.9
E18.5 3.2
E16.5 6.2
E14.5 9.6
E13.5 10.9
E12.5 9.2
E11.5 5.9
E10.5 6.8
Cell number (x10³)
C
Combined dataset
scRNAseq (68,366 cells)
UMAP
Full atlas
(= ovarian cells + mesonephros at E10.5-E11.5)
D
Stages
UMAP
E
Annotation
Luteal
MT
pre-Sup
pre-Gran
CE/SE
GM
gSP
MM
Gran
SLC
Stero
PV
SM
mSP
Eryt
Germ
AS
Immune
End
UMAP
Developing ovary (with mesonephros)
E10.5
E11.5
Ovary (without mesonephros)
E12.5 E14.5 E18.5 P5
E13.5 E16.5 P1 P56
Gata4+ domain = ovarian somatic cells
Annotated cell clusters
Epithelium
CE/SE
SLC/rete lineage
SLC
Supporting lineage
pre-Sup
pre-Gran
Gran
Steroidogenic/stromal lineages
GM
gSP
Stero
SM
PV
Corpus luteum
Luteal
Germ cell lineage
Germ
Mesonephric cells
MT
MM
mSP
Systemic cells
AS
End
Eryt
Immune
F
CE/SE pre-Sup pre-Gran Gran SLC GM gSP MM mSP Stero SM PV Luteal Germ MT AS End Eryt Immune
SE
Sup.
Stromal
Upk3b
Krt7
Wnt6
Lgr5
Bmp2
Foxl2
Pax8
Nr2f2
Tcf21
Wnt5a
Cyp11a1
Cyp17a1
Myh11
Mfap5
Rgs5
Mrap
Tinagl1
Dazl
Stra8
Pax2
Phox2b
Cdh5
Alas2
Rhd
Cd52
Gata4
Gata2
Mean expression
0 1
% of cells
20 40 60 80 100
Subset of ovarian somatic cells
(= CE/SE, SLC, pre-Sup, pre-Gran, Gran, GM, gSP, Stero, SM, PV)
G
cPAGA
Gran
pre-Gran
CE/SE
pre-Sup
SLC
Stero
gSP
PV
SM
H
E11.5 E12.5 E13.5 E14.5 E16.5 E18.5 P1 P5
pre-Sup gSP SLC CE
pre-Gran CE gSP SLC
CE gSP pre-Gran SLC
SLC CE gSP pre-Gran
CE pre-Gran PV SLC gSP
SE pre-Gran SLC gSP
SE gSP pre-Gran PV SLC
SE Gran SLC gSP PV SM
UMAP
I
Stages
1:CE/SE
2:SLC
42,199 cells
UMAP
J
Annotation
1:CE/SE
2:SLC
UMAP
K
Cell proportion
% of ovarian somatic cells
E10.5 E11.5 E12.5 E13.5 E14.5 E16.5 E18.5 P1 P5 P56
CE/SE
SLC
pre-Sup
pre-Gran
Gran
Sup.
GM
gSP
Stero
SM
PV
Luteal
Stromal
L
Cell proliferation
% of cells in G2/M
E10.5 E11.5 E12.5 E13.5 E14.5 E16.5 E18.5 P1 P5 P56

FIGURE 1

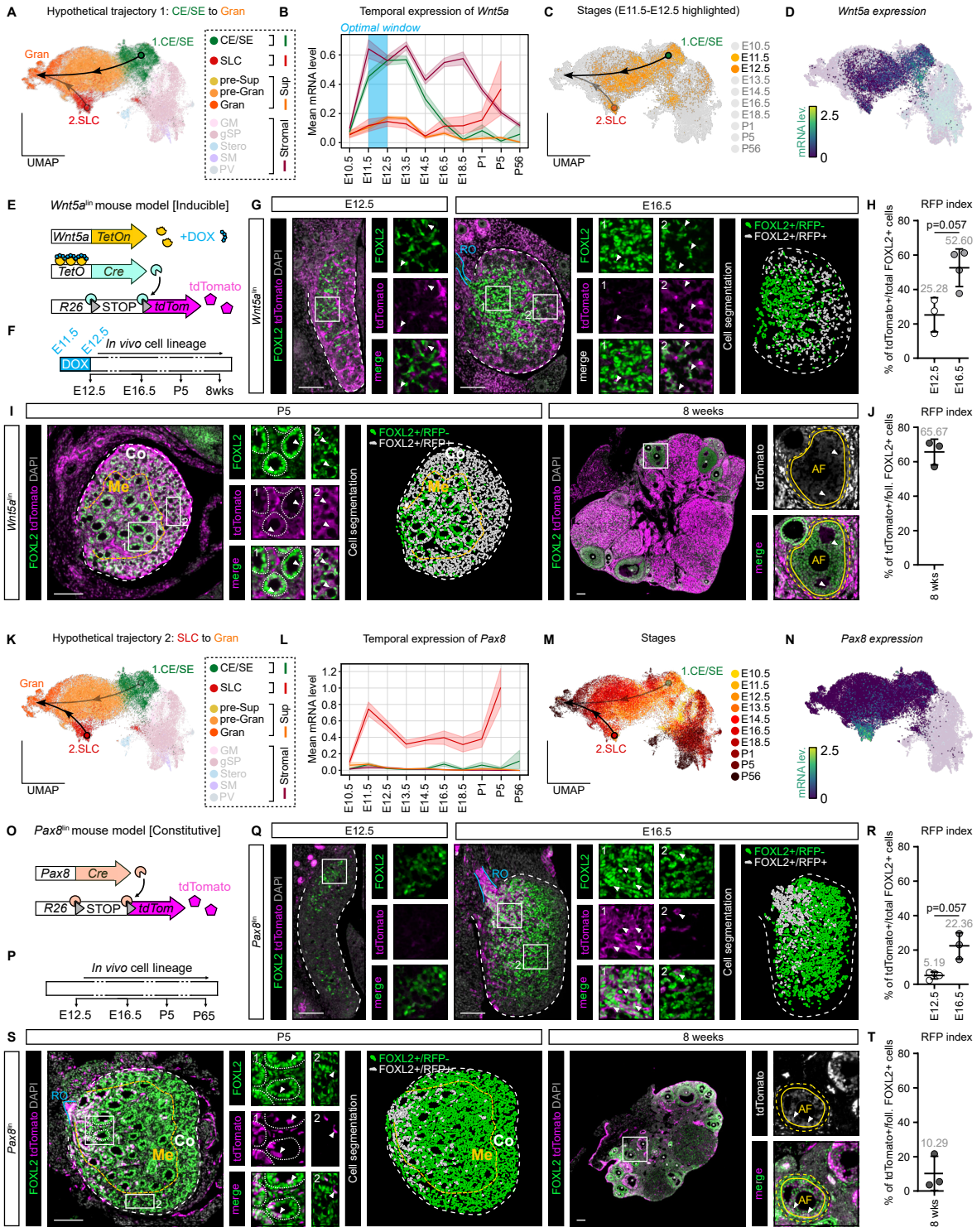
A
Hypothetical trajectory 1: CE/SE to Gran
Gran
1.CE/SE
2.SLC
UMAP
CE/SE
SLC
pre-Sup
pre-Gran
Gran
Sup
GM
gSP
Stero
SM
PV
Stromal
B
Temporal expression of Wnt5a
Optimal window
Mean mRNA level
C
Stages (E11.5-E12.5 highlighted)
E10.5
E11.5
E12.5
E13.5
E14.5
E16.5
E18.5
P1
P5
P56
D
Wnt5a expression
mRNA lev.
E
Wnt5a^lin mouse model [Inducible]
Wnt5a
TetOn
+DOX
TetO
Cre
tdTomato
R26
STOP
tdTom
F
In vivo cell lineage
DOX
E12.5
E16.5
P5
8wks
G
E12.5
E16.5
FOXL2
tdTomato
DAPI
merge
RO
Cell segmentation
FOXL2+/RFP-
FOXL2+/RFP+
H
RFP index
% of tdTomato+/total FOXL2+ cells
p=0.057
52.60
25.28
I
P5
8 weeks
Co
Me
AF
J
RFP index
% of tdTomato+/foll. FOXL2+ cells
65.67
8 wks
K
Hypothetical trajectory 2: SLC to Gran
L
Temporal expression of Pax8
M
Stages
N
Pax8 expression
O
Pax8^lin mouse model [Constitutive]
Pax8
Cre
P
In vivo cell lineage
P65
Q
R
p=0.057
22.36
5.19
S
T
10.29

FIGURE 2

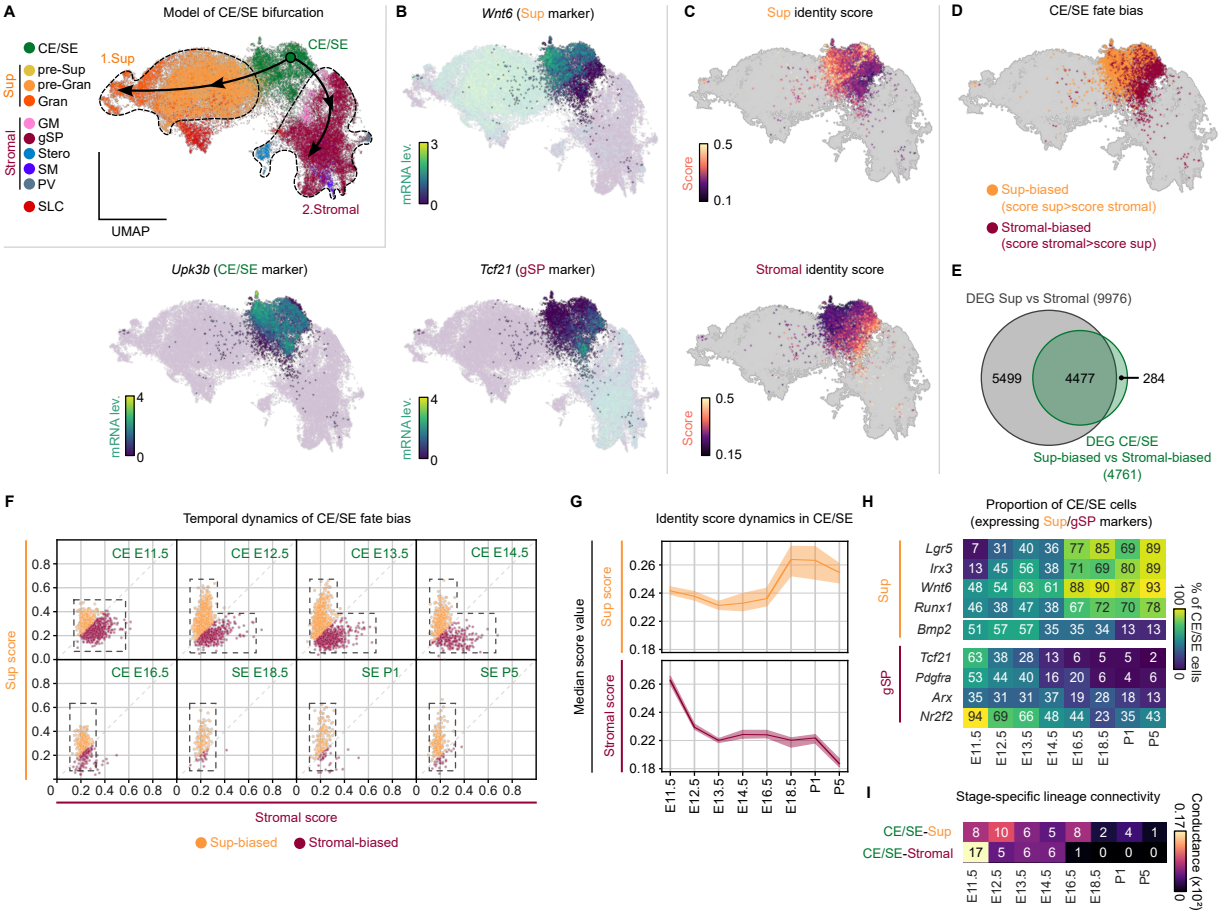
A
Model of CE/SE bifurcation
CE/SE
Sup
pre-Sup
pre-Gran
Gran
Stromal
GM
gSP
Stero
SM
PV
SLC
1.Sup
CE/SE
2.Stromal
UMAP
B
Wnt6 (Sup marker)
mRNA lev.
3
0
Upk3b (CE/SE marker)
mRNA lev.
4
0
Tcf21 (gSP marker)
mRNA lev.
4
0
C
Sup identity score
Score
0.5
0.1
Stromal identity score
Score
0.5
0.15
D
CE/SE fate bias
Sup-biased
(score sup>score stromal)
Stromal-biased
(score stromal>score sup)
E
DEG Sup vs Stromal (9976)
5499
4477
284
DEG CE/SE
Sup-biased vs Stromal-biased
(4761)
F
Temporal dynamics of CE/SE fate bias
CE E11.5
CE E12.5
CE E13.5
CE E14.5
CE E16.5
SE E18.5
SE P1
SE P5
Sup score
Stromal score
Sup-biased
Stromal-biased
G
Identity score dynamics in CE/SE
Median score value
Sup score
Stromal score
E11.5
E12.5
E13.5
E14.5
E16.5
E18.5
P1
P5
H
Proportion of CE/SE cells
(expressing Sup/gSP markers)
Sup
gSP
Lgr5 7 31 40 36 77 85 69 89
Irx3 13 45 56 38 71 69 80 89
Wnt6 48 54 63 61 88 90 87 93
Runx1 46 38 47 38 67 72 70 78
Bmp2 51 57 57 35 35 34 13 13
Tcf21 63 38 28 13 6 5 5 2
Pdgfra 53 44 40 16 20 6 4 6
Arx 35 31 31 37 19 28 18 13
Nr2f2 94 69 66 48 44 23 35 43
% of CE/SE cells
100
0
I
Stage-specific lineage connectivity
CE/SE-Sup 8 10 6 5 8 2 4 1
CE/SE-Stromal 17 5 6 6 1 0 0 0
Conductance (x10²)
0.17
0

FIGURE 3

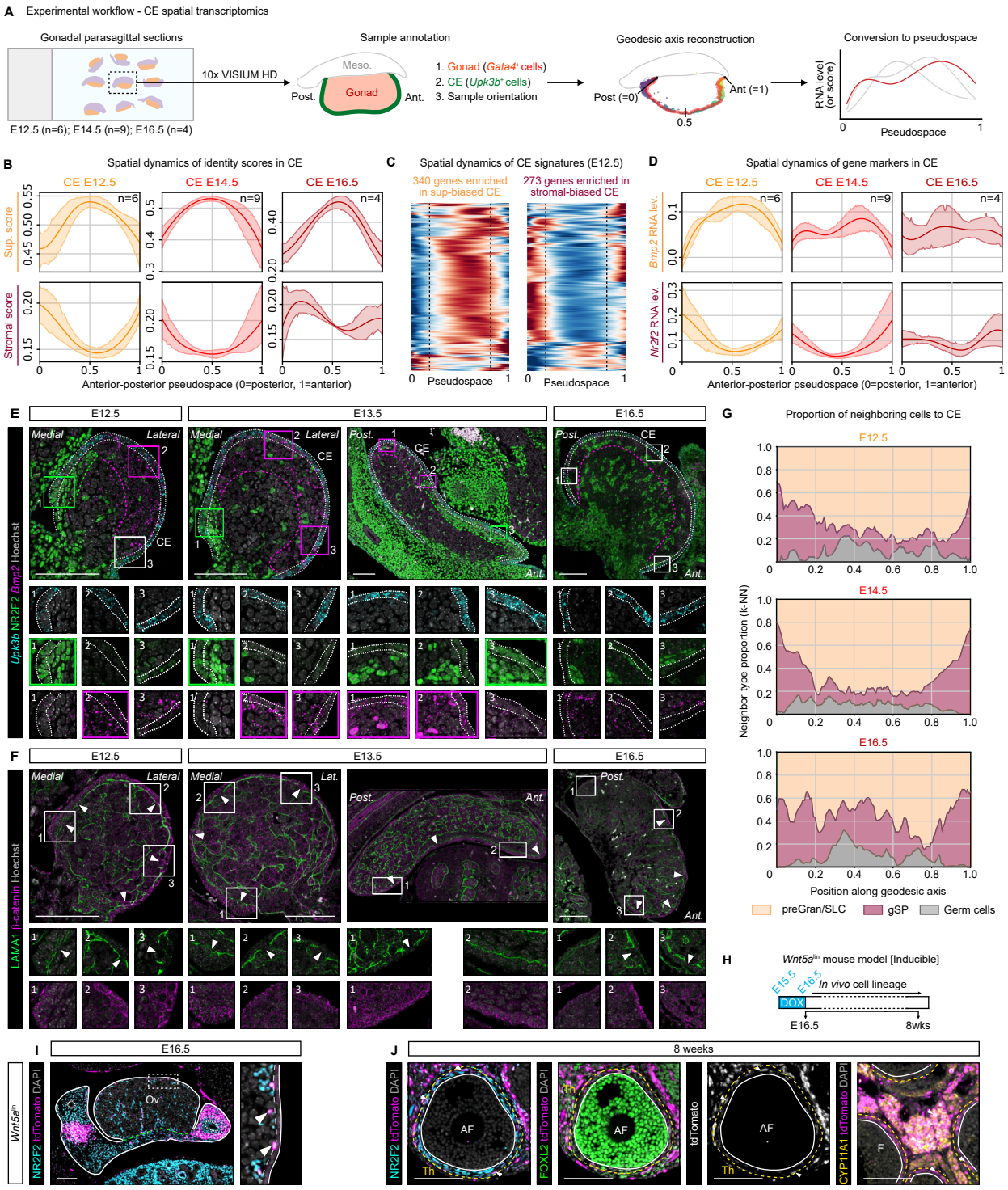
A
Experimental workflow - CE spatial transcriptomics
Gonadal parasagittal sections
10x VISIUM HD
E12.5 (n=6); E14.5 (n=9); E16.5 (n=4)
Sample annotation
Meso.
Post.
Gonad
Ant.
1. Gonad (Gata4+ cells)
2. CE (Upk3b+ cells)
3. Sample orientation
Geodesic axis reconstruction
Post (=0)
Ant (=1)
0.5
Conversion to pseudospace
RNA level (or score)
Pseudospace
B
Spatial dynamics of identity scores in CE
CE E12.5
CE E14.5
CE E16.5
Sup. score
Stromal score
Anterior-posterior pseudospace (0=posterior, 1=anterior)
C
Spatial dynamics of CE signatures (E12.5)
340 genes enriched in sup-biased CE
273 genes enriched in stromal-biased CE
Pseudospace
D
Spatial dynamics of gene markers in CE
Bmp2 RNA lev.
Nr2f2 RNA lev.
Anterior-posterior pseudospace (0=posterior, 1=anterior)
E
E12.5
E13.5
E16.5
Medial
Lateral
Post.
Ant.
CE
Upk3b NR2F2 Bmp2 Hoechst
F
LAMA1 β-catenin Hoechst
G
Proportion of neighboring cells to CE
Neighbor type proportion (k-NN)
Position along geodesic axis
preGran/SLC
gSP
Germ cells
H
Wnt5a^in mouse model [Inducible]
In vivo cell lineage
DOX
E15.5
E16.5
8wks
I
Wnt5a^in
NR2F2 tdTomato DAPI
Ov
J
8 weeks
NR2F2 tdTomato DAPI
FOXL2 tdTomato DAPI
tdTomato
CYP11A1 tdTomato DAPI
AF
Th
F

FIGURE 4

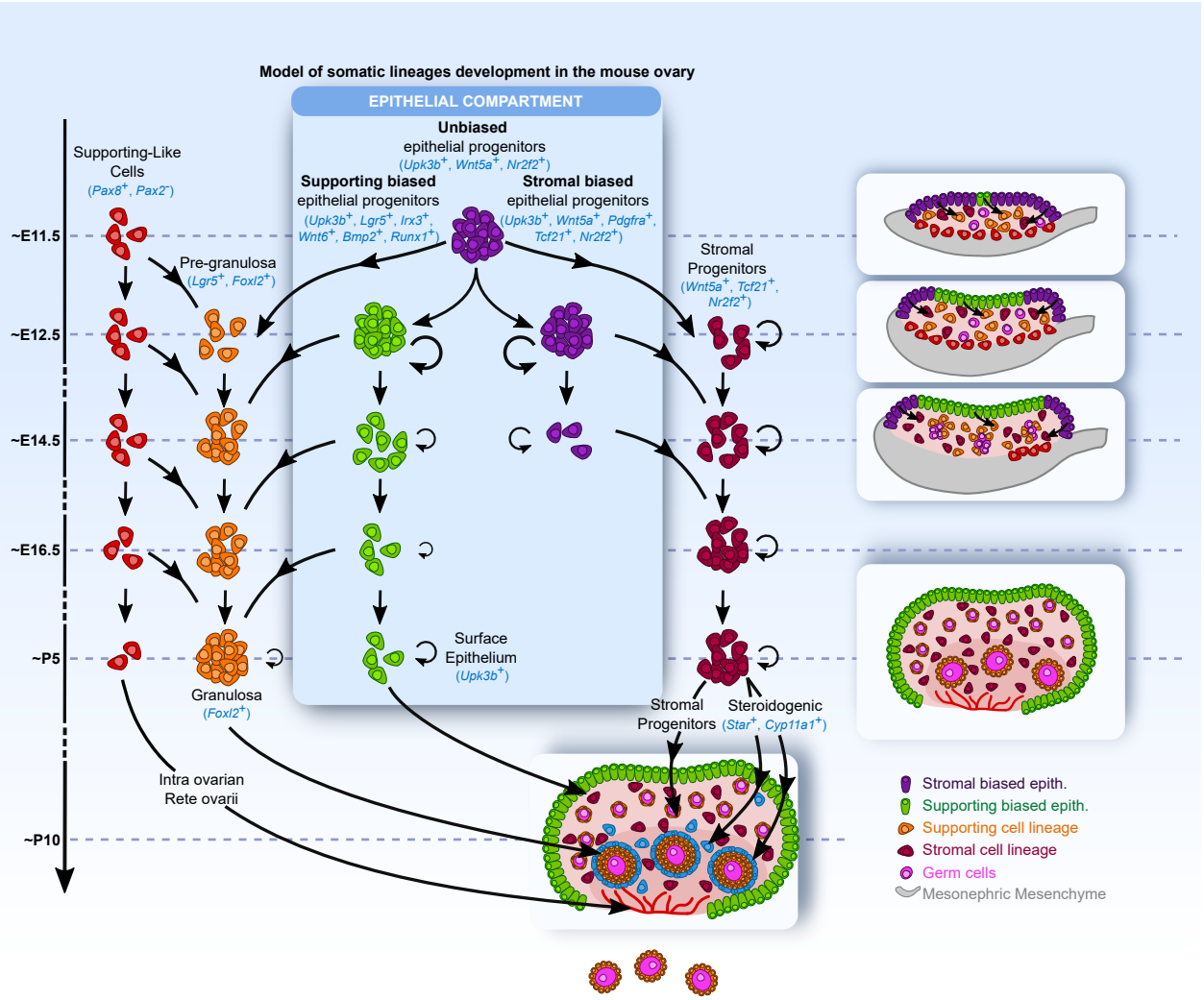
Model of somatic lineages development in the mouse ovary
EPITHELIAL COMPARTMENT
Unbiased
epithelial progenitors
(Upk3b+, Wnt5a+, Nr2f2+)
Supporting biased
epithelial progenitors
(Upk3b+, Lgr5+, Irx3+, Wnt6+, Bmp2+, Runx1+)
Stromal biased
epithelial progenitors
(Upk3b+, Wnt5a+, Pdgfra+, Tcf21+, Nr2f2+)
Supporting-Like Cells
(Pax8+, Pax2-)
Pre-granulosa
(Lgr5+, Foxl2+)
Stromal Progenitors
(Wnt5a+, Tcf21+, Nr2f2+)
~E11.5
~E12.5
~E14.5
~E16.5
~P5
~P10
Surface Epithelium
(Upk3b+)
Granulosa
(Foxl2+)
Stromal Progenitors
Steroidogenic
(Star+, Cyp11a1+)
Intra ovarian Rete ovarii
Stromal biased epith.
Supporting biased epith.
Supporting cell lineage
Stromal cell lineage
Germ cells
Mesonephric Mesenchyme

FIGURE 5

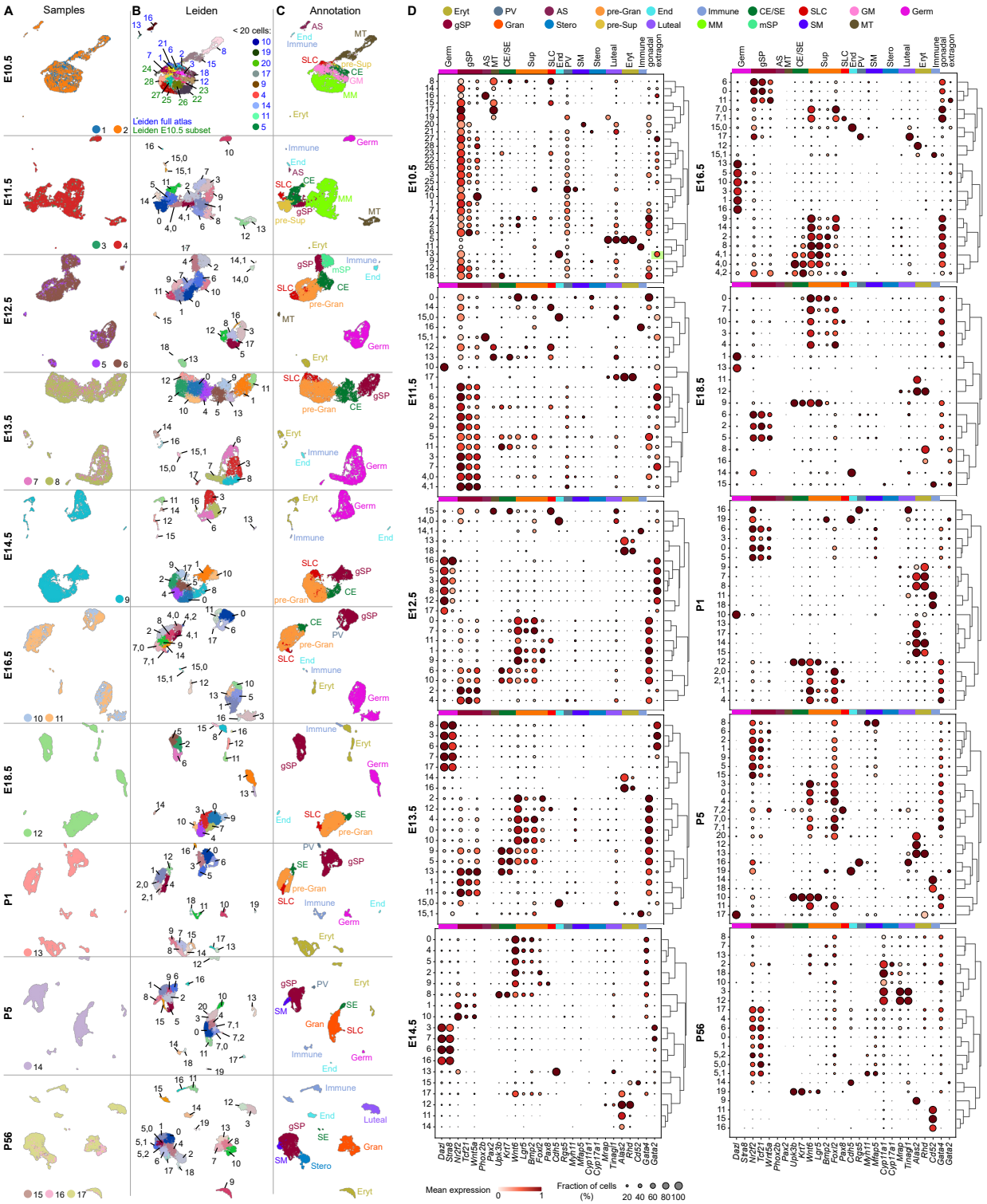
A
Samples
B
Leiden
C
Annotation
D
E10.5
E11.5
E12.5
E13.5
E14.5
E16.5
E18.5
P1
P5
P56
< 20 cells:
Leiden full atlas
Leiden E10.5 subset
Eryt
gSP
PV
Gran
AS
Stero
pre-Gran
pre-Sup
End
Luteal
Immune
MM
CE/SE
mSP
SLC
SM
GM
MT
Germ
Mean expression
Fraction of cells (%)

FIGURE S1

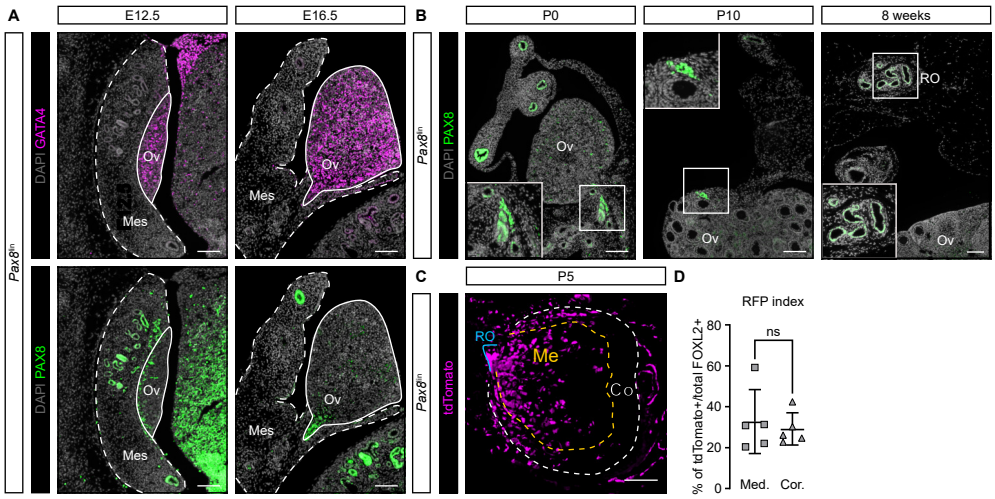
A
E12.5
E16.5
B
P0
P10
8 weeks
Pax8in
DAPI GATA4
DAPI PAX8
Ov
Mes
RO
C
P5
D
tdTomato
Me
Co
RFP index
ns
% of tdTomato+/total FOXL2+
80
60
40
20
0
Med.
Cor.

FIGURE S2

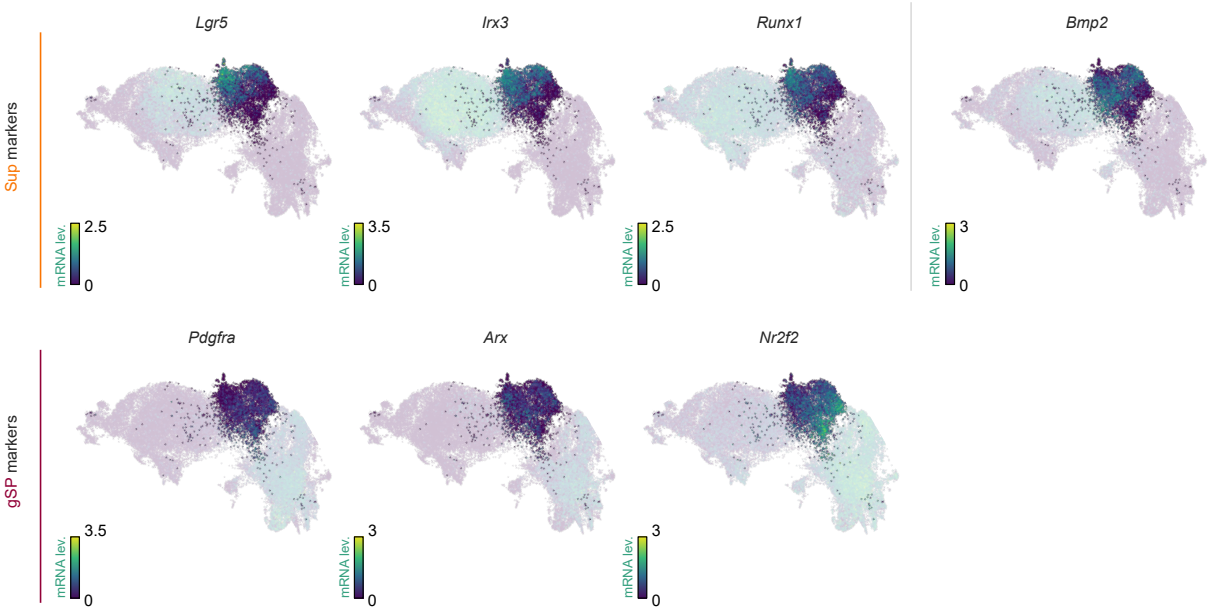
Sup markers
Lgr5
Irx3
Runx1
Bmp2
mRNA lev.
2.5
0
3.5
0
2.5
0
3
0
gSP markers
Pdgfra
Arx
Nr2f2
mRNA lev.
3.5
0
3
0
3
0

FIGURE S3

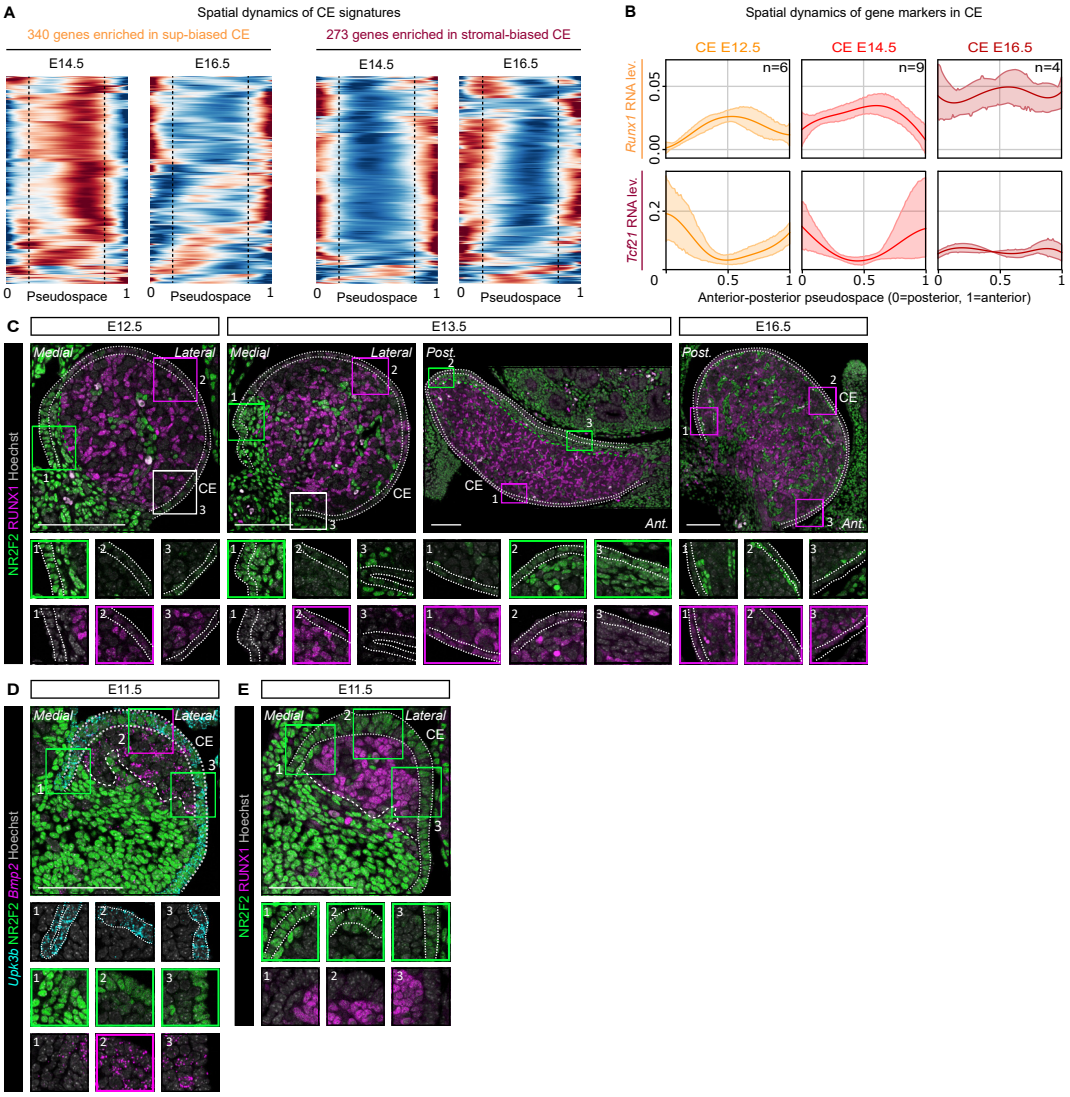
A
Spatial dynamics of CE signatures
340 genes enriched in sup-biased CE
273 genes enriched in stromal-biased CE
E14.5
E16.5
E14.5
E16.5
0
Pseudospace
1
B
Spatial dynamics of gene markers in CE
CE E12.5
CE E14.5
CE E16.5
n=6
n=9
n=4
Runx1 RNA lev.
Tcf21 RNA lev.
Anterior-posterior pseudospace (0=posterior, 1=anterior)
C
E12.5
E13.5
E16.5
Medial
Lateral
Post.
Ant.
CE
NR2F2 RUNX1 Hoechst
D
E11.5
Upk3b NR2F2 Bmp2 Hoechst
E
E11.5
NR2F2 RUNX1 Hoechst

FIGURE S4